



Fourth-Order Conservative Non-splitting Semi-Lagrangian Hermite WENO Schemes for Kinetic and Fluid Simulations

Nanyi Zheng¹ · Xiaofeng Cai^{2,3} · Jing-Mei Qiu⁴ · Jianxian Qiu⁵

Received: 20 August 2023 / Revised: 11 January 2024 / Accepted: 22 February 2024 /

Published online: 29 April 2024

© The Author(s) 2024

Abstract

We present fourth-order conservative non-splitting semi-Lagrangian (SL) Hermite essentially non-oscillatory (HWENO) schemes for linear transport equations with applications for nonlinear problems including the Vlasov–Poisson system, the guiding center Vlasov model, and the incompressible Euler equations in the vorticity-stream function formulation. The proposed SL HWENO schemes combine a weak formulation of the characteristic Galerkin method with two newly constructed HWENO reconstruction methods. The new HWENO reconstructions are meticulously designed to strike a delicate balance between curbing numerical oscillation and introducing excessive dissipation. Mass conservation naturally holds due to the weak formulation of the semi-Lagrangian discontinuous Galerkin method and the design of the HWENO reconstructions. We apply a positivity-preserving limiter to maintain the positivity of numerical solutions when needed. Abundant benchmark tests are performed to verify the effectiveness of the proposed SL HWENO schemes.

Keywords Positivity preservation · Non-splitting scheme · Conservative semi-Lagrangian · HWENO reconstruction · Vlasov systems · Incompressible flows

✉ Xiaofeng Cai
xfcai@bnu.edu.cn

Nanyi Zheng
nyzheng@stu.xmu.edu.cn

Jing-Mei Qiu
jingqiu@udel.edu

Jianxian Qiu
jxqiu@xmu.edu.cn

¹ School of Mathematical Sciences, Xiamen University, Xiamen 361005, Fujian, China

² Research Center for Mathematics, Advanced Institute of Natural Sciences, Beijing Normal University, Zhuhai 519087, China

³ Guangdong Provincial Key Laboratory of Interdisciplinary Research and Application for Data Science, BNU-HKBU United International College, Zhuhai 519087, China

⁴ Department of Mathematical Sciences, University of Delaware, Newark, DE 19716, USA

⁵ School of Mathematical Sciences and Fujian Provincial Key Laboratory of Mathematical Modeling and High-Performance Scientific Computing, Xiamen University, Xiamen 361005, Fujian, China

1 Introduction

The transport equation in the form of

$$u_t + \nabla_{\mathbf{x}} \cdot (\mathbf{a}(u, \mathbf{x}, t)u) = 0, \quad (1.1)$$

where $u(\mathbf{x}, t)$ usually represents a density function of a conservative quantity in a velocity field $\mathbf{a}(u, \mathbf{x}, t)$ with $\mathbf{x} \in \mathbb{R}^d$, which is widely used in fluid mechanics and kinetic models.

Three popular approaches including the Eulerian approach, the Lagrangian approach, and the semi-Lagrangian (SL) approach have been proposed for solving the transport problems. Comparing with the Eulerian and the Lagrangian approaches, the SL approach naturally holds its advantages in terms of accuracy and efficiency for certain applicable problems. On one hand, the same with the Lagrangian approach, the SL approach evaluates the solution along the convection characteristics. Hence, it allows large numerical time steps comparing with the Eulerian approach. On the other hand, as the Eulerian approach, the SL approach adopts a fixed spatial mesh equipped with a wide range of different solution spaces for high-order spatial accuracy. As a comparison, the Lagrangian approach suffers from statistical noise and only achieves a low order of $O(1/\sqrt{N})$ with N representing the number of sampling points.

It is challenging to efficiently simulate the transport problems, due to their complicated solution structures such as discontinuity, filamentation; for instance, the Vlasov–Poisson system has drastic high-frequency filamentation structures [29, 31] and the guiding center Vlasov model has steep structures [35]. To handle such complicated structures, the SL approach has been coupled with the discontinuous Galerkin (DG) method [22, 29, 30], the weighted essentially non-oscillatory (WENO) schemes [18, 28, 34], and the Hermite WENO (HWENO) schemes [6, 36, 40]. For the DG method, it needs many degrees of freedom (DOF) per element for its high-order version, especially in a high-dimension setting. For high-order WENO schemes, they always require very wide reconstruction stencils, compared with the DG method. The HWENO methods can be regarded as an intermediate transition from the DG method to a WENO method. It requires significantly fewer degrees of freedom per element compared with the DG method, and it uses a more compact stencil for high-order reconstruction compared with the WENO method. Considering the high dimension of the Vlasov–Poisson system, developing high-resolution Hermite WENO schemes in the framework of the SL scheme is necessary for an efficient Vlasov solver with large time step and high order accuracy.

The HWENO method was first introduced by Qiu and Shu in [26] and was further developed in [7, 11, 27, 39], which is shown to be more accurate than the same-order WENO scheme. Notice that the HWENO schemes in [7, 11, 26, 27] use point-wise positive linear weights to present the information of a high-degree polynomial as a convex combination of the information of several low-degree polynomials. In [7, 11, 26, 27], such positive linear weights do exist for the specific Gaussian points they require. However, one can find that such positive linear weights do not exist for some special locations (even regions) in an Eulerian grid for each HWENO reconstruction in [7, 11, 26, 27]. Notice that characteristic feet for (1.1) can be located anywhere on an Eulerian grid; and the reconstruction designs in [7, 11, 26, 27] are not suitable for an SL method. Based on the observation above, in our previous work [40], we adopted a 1-D hybrid HWENO reconstruction method proposed in [39], and developed a dimensional-splitting SL hybrid HWENO scheme.

In our earlier work [41], we proposed fourth-order, locally conservative, non-splitting semi-Lagrangian finite volume WENO schemes for 2D linear transport equation and non-linear Vlasov dynamics. The first aim of this paper is to incorporate the recently developed HWENO reconstruction method in [39] denoted as HWENO-3 into this spatiotemporal semi-

Lagrangian framework [41]. The new SL HWENO schemes do not rely on operator splitting. One significant benefit of a non-splitting SL method is that it remains its designed temporal order of accuracy for strongly nonlinear transport equations (in which the velocity field is hard to be decoupled). For some nonlinear problems, splitting-based SL method suffers from a first-order temporal error [41].

In the simulations of this paper, we find that the HWENO-3 is very dissipative for the filamentation structures that including large-gradient extreme points. It leads to the second aim of this paper: to propose new HWENO reconstruction methods that overcome the dissipation nature of the HWENO-3 in [39]. One can also refer to splitting SL HWENO-3 in [40] and clearly observe that the dissipation of the HWENO-3 method negatively affects the accuracy of the swirling deformation flow test. To overcome the dissipation issue, we propose two new two-dimensional (2-D) HWENO reconstruction methods, denoted by HWENO-1 and HWENO-2. Comparing with the HWENO reconstruction technique in [39], a key difference of the newly constructed reconstructions is that we rule out the participation of any first-degree polynomial, which leads to large numerical dissipation. The two newly proposed HWENO methods gather information from central or one-sided constructed polynomials, which are at least quadratic. Theoretically, a good HWENO reconstruction approximates the highest-degree polynomial where the solution is continuous and reduces to a one-sided lower-degree polynomial when a discontinuity is involved. To achieve such a principle, we propose two different strategies. For the HWENO-1, we follow the same technique in [39], but based on newly chosen polynomials. The resulting HWENO-1 method has a significant improvement in reducing numerical dissipation. On the other hand, the HWENO-2 directly selects one polynomial from all candidates. This is equivalent to assigning weights of one or zero to candidate polynomials. The stencil selection strategy of the HWENO-2 is motivated by the targeted essentially non-oscillatory (TENO) schemes developed by Fu et al. [14–16]. Recently, a Hermite TENO (HTENO) is developed in [19], which presents very good numerical results. There are two reasons not to apply the HTENO method in [19]. Firstly, it depends on point-wise positive linear weights as we mentioned before. Secondly, it is only a one-dimensional version method. Both the HWENO-1 and HWENO-2 have a huge improvement in terms of dissipation comparing with the HWENO reconstruction in [39]. But, there are subtle differences in effectiveness. On one hand, the HWENO-1 is “smoother” due to its nature of assigning non-zero weight to each candidate polynomial. As a comparison, the HWENO-2 (or HTENO) only chooses one candidate, which means the piecewise polynomial constructed by the HWENO-2 can be fragmented sometimes. On the other hand, the HWENO-2 is more robust for capturing discontinuity since the highest-degree polynomial is not involved at all as long as the stencil selecting strategy works correctly. In this paper, we will describe the construction of the HWENO-1 and HWENO-2 in details and compare these two strategies by extensive numerical tests.

The proposed non-splitting SL HWENO schemes incorporate the local adjoint problems, drawing from both the SL DG methods [4, 5, 17] and the Eulerian-Lagrangian localized adjoint methods (ELLAM) [10, 32]. This integration is utilized to update the zeroth-order and first-order moments. In other words, we define the solution space as a P^1 DG space. However, through the HWENO reconstructions, the P^1 DG solution is replaced with a piecewise P^3 polynomial for the solution evaluation. Such a procedure can be viewed as a $P_N P_M$ method introduced in [12]. The combination of the weak formulation of SL DG method and the HWENO reconstruction can also be regarded as a one-step evolution Galerkin scheme introduced in [24]. The proposed SL scheme requires a remapping procedure between a fixed Eulerian mesh and a characteristic upstream twisted mesh. To achieve a fourth-order accuracy, the remapping procedure can be summarized in the following three steps. Firstly, we define

a cubic-curved numerical upstream mesh to approximate the real upstream mesh. Secondly, a clipping technique is involved to gather the curved polygons generated from the Eulerian mesh and the cubic-curved mesh. Finally, apply piecewise integration over each cubic-curved upstream cell. For nonlinear models, we couple the proposed SL HWENO schemes with the fourth-order Runge–Kutta exponential integrator (RKEI) [9], which freezes the velocity field for each stage, for high-order temporal accuracy. Notice that the evaluation of zeroth-order moment (cell average) is equivalent to the formulation of the SL finite volume (FV) method in [41]. The mass conservation, positivity preservation (PP), and fourth-order accuracy of the proposed schemes can be proved, similar to [41]. For stability, under a linearized setting, we numerically prove the unconditionally stable property of the proposed schemes by the Fourier analysis.

An outline of this paper is as follows. In Sect. 2, we introduce the construction of the SL HWENO schemes. In Sect. 3, we describe how to couple the proposed SL HWENO scheme with the fourth-order RKEI method for nonlinear models. A variety of numerical tests are provided in Sect. 4. Finally, a conclusion is presented in Sect. 5.

2 Two-Dimensional SL HWENO Schemes

Consider the following linear transport equation

$$u_t + (a(x, y, t)u)_x + (b(x, y, t)u)_y = 0, \quad (2.1)$$

where $(a(x, y, t), b(x, y, t))$ represents a known velocity field and $u(x, y, t)$ is a density function. We assume a rectangle computational domain $\Omega := [x_L, x_R] \times [y_B, y_T]$ and a corresponding discretization such that $x_L = x_{\frac{1}{2}} < x_{\frac{3}{2}} < \dots < x_{N_x+\frac{1}{2}} = x_R$, $y_B = y_{\frac{1}{2}} < y_{\frac{3}{2}} < \dots < y_{N_y+\frac{1}{2}} = y_T$, with $I_i^x := \left[x_{i-\frac{1}{2}}, x_{i+\frac{1}{2}} \right]$, $I_j^y := \left[y_{j-\frac{1}{2}}, y_{j+\frac{1}{2}} \right]$, $I_{i,j} := I_i^x \times I_j^y$, $x_i := \frac{x_{i-\frac{1}{2}}+x_{i+\frac{1}{2}}}{2}$, $y_j := \frac{y_{j-\frac{1}{2}}+y_{j+\frac{1}{2}}}{2}$, $\Delta x_i := x_{i+\frac{1}{2}} - x_{i-\frac{1}{2}}$ and $\Delta y_j := y_{j+\frac{1}{2}} - y_{j-\frac{1}{2}}$. We define a P^1 DG solution space $V_h^1 := \{u_h | u_h(x, y)|_{I_{i,j}} \in P^1(I_{i,j}) \forall i, j\}$. Consider an Eulerian cell $I_{i,j}$ at $t = t^{n+1}$ and define a dynamic characteristic region $I_{i,j}(t) := \{(x^*, y^*) | (x^*, y^*) = (X(x, y; t), Y(x, y; t)), (x, y) \in I_{i,j}\}$, where $(X(x, y; t), Y(x, y; t))$ represents the characteristic curve emanating from (x, y, t^{n+1}) , i.e., the solution of the ordinary differential equations (ODEs)

$$\begin{cases} dX(t)/dt = a(X(t), Y(t), t), \\ dY(t)/dt = b(X(t), Y(t), t), \\ X(t^{n+1}) = x, \\ Y(t^{n+1}) = y. \end{cases} \quad (2.2)$$

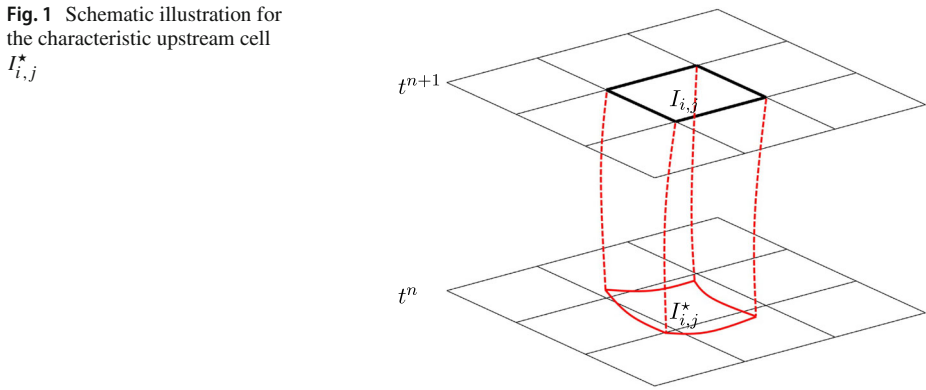
We define an adjoint problem of (2.1) as in [4] on $I_{i,j}(t) \times [t^n, t^{n+1}]$: for a given test function $W(x, y) \in P^1(I_{i,j})$,

$$\begin{cases} w_t + a(x, y, t)w_x + b(x, y, t)w_y = 0, & t \in [t^n, t^{n+1}] \\ w(t = t^{n+1}) = W(x, y). \end{cases} \quad (2.3)$$

By the Reynolds transport Theorem, we have,

$$\frac{d}{dt} \iint_{I_{i,j}(t)} u(x, y, t)w(x, y, t) dx dy = 0. \quad (2.4)$$

Fig. 1 Schematic illustration for the characteristic upstream cell $I_{i,j}^*$



From (2.4), an SL scheme is naturally formulated:

$$\frac{1}{\Delta x_i \Delta y_j} \iint_{I_{i,j}} u(x, y, t^{n+1}) W(x, y) dx dy = \frac{1}{\Delta x_i \Delta y_j} \iint_{I_{i,j}^*} u(x, y, t^n) w(x, y, t^n) dx dy, \quad (2.5)$$

where $I_{i,j}^* = I_{i,j}(t^n)$ (see Fig. 1).

For given time level t^n , we denote the first three moments of the solution by $\{\bar{u}_{i,j}\}$, $\{\bar{v}_{i,j}\}$, and $\{\bar{w}_{i,j}\}$. Then, we denote the numerical solution on t^n by u^n with

$$u^n(x, y) = \bar{u}_{i,j} + 12\bar{v}_{i,j} \left(\frac{x - x_i}{\Delta x_i} \right) + 12\bar{w}_{i,j} \left(\frac{y - y_j}{\Delta y_j} \right), \quad (x, y) \in I_{i,j}. \quad (2.6)$$

For constructing an SL HWENO scheme, it is sufficient to take $W(x, y) = 1$, $(x - x_i)/\Delta x_i$, $(y - y_j)/\Delta y_j$ and evaluate the right-hand side of (2.5) accurately. To approximate the right-hand side of (2.5), in Sect. 2.1, we first introduce the two newly constructed HWENO reconstructions to recover a piecewise cubic polynomial, denoted by $H^n(x, y)$, to approximate $u(x, y, t^n)$ in (2.5). Then, in Sect. 2.2, cubic-curved quadrilaterals, denoted by $\{\tilde{I}_{i,j}^*\}$, are defined for approximating $\{I_{i,j}^*\}$ and a cubic polynomial $\tilde{w}(x, y)$ is constructed over each $\tilde{I}_{i,j}^*$ by a least square procedure to approximate the test function $w(x, y)$. Finally, we briefly summarize the integration strategy on $\tilde{I}_{i,j}^*$ in Sect. 2.3.

2.1 Two-Dimensional HWENO Reconstruction Methods

For convenience, we require $\Delta x_i \equiv \Delta x$, $\Delta y_j \equiv \Delta y$, $\forall i, j$. Based on the P^1 DG solution, $u^n(x, y)$, we recover a piecewise P^3 polynomial,

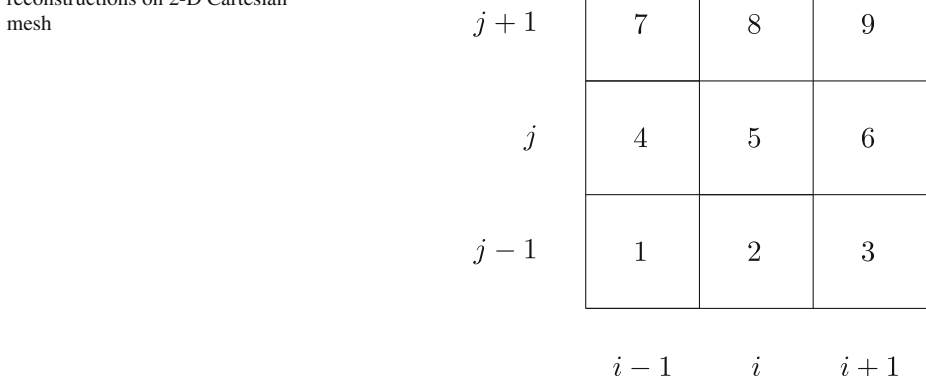
$$H^n(x, y) = H^{(i,j)}(x, y), \quad (x, y) \in I_{i,j}, \quad \forall (i, j), \quad (2.7)$$

where $H^{(i,j)}(x, y) \in P^3(I_{i,j})$. We define a set of local orthogonal basis of the high order polynomial denoted as $\{P_l(x, y)\}$ with:

$$P_1(x, y) = 1, \quad P_2(x, y) = \mu_i(x) := \frac{x - x_i}{\Delta x}, \quad P_3(x, y) = v_j(y) := \frac{y - y_j}{\Delta y},$$

$$P_4(x, y) = \mu_i^2 - \frac{1}{12}, \quad P_5(x, y) = \mu_i v_j, \quad P_6(x, y) = v_j^2 - \frac{1}{12},$$

Fig. 2 Stencil for the HWENO reconstructions on 2-D Cartesian mesh



$$\begin{aligned} P_7(x, y) &= \mu_i^3 - \frac{3}{20}\mu_i, \quad P_8(x, y) = \left(\mu_i^2 - \frac{1}{12}\right)v_j, \quad P_9(x, y) = \mu_i \left(v_j^2 - \frac{1}{12}\right), \\ P_{10}(x, y) &= v_j^3 - \frac{3}{20}v_j, \quad P_{11}(x, y) = \left(\mu_i^2 - \frac{1}{12}\right)\left(v_j^2 - \frac{1}{12}\right). \end{aligned} \quad (2.8)$$

We also define that $\bar{u}_5^n := \bar{u}_{i,j}^n$, $\bar{v}_5^n := \bar{v}_{i,j}^n$, $\bar{w}_5^n := \bar{w}_{i,j}^n$, $I_5 := I_{i,j}$ and other $\{\bar{u}_s^n\}$, $\{\bar{v}_s^n\}$, $\{\bar{w}_s^n\}$, $\{I_s\}$ represent corresponding moments and Eulerian cells based on the serial numbers in Fig. 2. Then, the 2-D HWENO reconstruction methods over $I_{i,j}$ are summarized as follows.

Step 1. Reconstruct the first-order moments.

The first-order moments, $\{\bar{v}_5^n, \bar{w}_5^n\}$, can be extremely large when $u(x, y, t^n)$ is discontinuous in $I_{i,j}$ since $\bar{v}_5^n \sim \frac{\Delta x}{12} \frac{\partial u}{\partial x}|_{(x_i, y_j)}$ and $\bar{w}_5^n \sim \frac{\Delta y}{12} \frac{\partial u}{\partial y}|_{(x_i, y_j)}$. Hence, before recovering a cubic polynomial, we reconstruct the first-order moments with the following two goals: it will provide high-order approximations of first-order moments when $u(x, y, t^n)$ is smooth in $I_{i,j}$; when $u(x, y, t^n)$ is discontinuous in $I_{i,j}$, first-order moments will be reduced to a reasonable level.

The two first-order moments can be regarded as local indicators of the changing rates for the x - and y -dimensions. Each of them is highly independent of the other dimension. Hence, the reconstruction is performed in a dimension-by-dimension manner. Below, we take the x direction as an example to illustrate the procedure for reconstructing its first-order moment.

Step 1.1. Compute approximations to the first-order moment and smoothness indicators from 1-D polynomial reconstructions.

1. Construct a quartic polynomial $p_0(x)$, and three quadratic polynomials $\{p_k(x)\}_{k=1}^3$ satisfying

$$\begin{aligned} \frac{1}{\Delta x} \int_{I_{i+l}^x} p_0(x) dx &= \bar{u}_{i+l,j}^n, \quad l = -1, 0, 1, \\ \frac{1}{\Delta x} \int_{I_{i+l}^x} p_0(x) \left(\frac{x - x_{i+l}}{\Delta x}\right) dx &= \bar{v}_{i+l,j}^n, \quad l = -1, 1, \end{aligned} \quad (2.9)$$

and

$$\begin{aligned} \frac{1}{\Delta x} \int_{I_{i+l}^x} p_1(x) dx &= \bar{u}_{i+l,j}^n, \quad l = -1, 0, \quad \frac{1}{\Delta x} \int_{I_{i-1}^x} p_1(x) \left(\frac{x - x_{i-1}}{\Delta x} \right) dx = \bar{v}_{i-1,j}^n, \\ \frac{1}{\Delta x} \int_{I_{i+l}^x} p_2(x) dx &= \bar{u}_{i+l,j}^n, \quad l = -1, 0, 1, \\ \frac{1}{\Delta x} \int_{I_{i+l}^x} p_3(x) dx &= \bar{u}_{i+l,j}^n, \quad l = 0, 1, \quad \frac{1}{\Delta x} \int_{I_{i+1}^x} p_3(x) \left(\frac{x - x_{i+1}}{\Delta x} \right) dx = \bar{v}_{i+1,j}^n. \end{aligned} \quad (2.10)$$

2. Compute the first-order moments of $\{p_k(x)\}_{k=0}^3$:

$$\begin{aligned} \tilde{v}_{i,j,0}^n &:= \frac{1}{\Delta x} \int_{I_i^x} p_0(x) \left(\frac{x - x_i}{\Delta x} \right) dx = -\frac{5}{76} \bar{u}_{i-1,j}^n - \frac{11}{38} \bar{v}_{i-1,j}^n \\ &\quad - \frac{11}{38} \bar{v}_{i+1,j}^n + \frac{5}{76} \bar{u}_{i+1,j}^n, \\ \tilde{v}_{i,j,1}^n &:= \frac{1}{\Delta x} \int_{I_i^x} p_1(x) \left(\frac{x - x_i}{\Delta x} \right) dx = \frac{1}{6} \bar{u}_{i,j}^n - \frac{1}{6} \bar{u}_{i-1,j}^n - \bar{v}_{i-1,j}^n, \\ \tilde{v}_{i,j,2}^n &:= \frac{1}{\Delta x} \int_{I_i^x} p_2(x) \left(\frac{x - x_i}{\Delta x} \right) dx = \frac{1}{24} \bar{u}_{i+1,j}^n - \frac{1}{24} \bar{u}_{i-1,j}^n, \\ \tilde{v}_{i,j,3}^n &:= \frac{1}{\Delta x} \int_{I_i^x} p_3(x) \left(\frac{x - x_i}{\Delta x} \right) dx = \frac{1}{6} \bar{u}_{i+1,j}^n - \frac{1}{6} \bar{u}_{i,j}^n - \bar{v}_{i+1,j}^n. \end{aligned} \quad (2.11)$$

3. Compute the smoothness indicators $\{\beta_k\}_{k=0}^3$ of $\{p_k(x)\}_{k=0}^3$ [20, 23, 33]:

$$\beta_k = \sum_{l=1}^r \frac{1}{\Delta x} \int_{I_i^x} \left(\Delta x^l \frac{\partial^l}{\partial x^l} p_k(x) \right)^2 dx, \quad k = 0, 1, 2, 3 \quad (2.12)$$

with r representing the degree of the corresponding polynomial. Here, the smoothness indicators $\{\beta_k\}_{k=1}^3$ can be explicitly expressed by

$$\begin{aligned} \beta_1 &= \left(12 \tilde{v}_{i,j,1}^n \right)^2 + 156 \left(\tilde{v}_{i,j,1}^n - \bar{v}_{i-1,j}^n \right)^2, \\ \beta_2 &= \left(12 \tilde{v}_{i,j,2}^n \right)^2 + \frac{13}{12} \left(\bar{u}_{i+1,j}^n - 2\bar{u}_{i,j}^n + \bar{u}_{i-1,j}^n \right)^2, \\ \beta_3 &= \left(12 \tilde{v}_{i,j,3}^n \right)^2 + 156 \left(\bar{v}_{i+1,j}^n - \tilde{v}_{i,j,3}^n \right)^2. \end{aligned} \quad (2.13)$$

We refer to [39] for the explicit expression of β_0 .

4. Compute a full stencil global reference smoothness indicator [19]:

$$\tau := \left(\frac{|\beta_0 - \beta_1| + |\beta_0 - \beta_3|}{2} \right)^2. \quad (2.14)$$

By the Taylor expansion, we can find that $\tau = O(\Delta x^6)$, if there is no discontinuity involved.

Step 1.2. Weight the collected first-order moments.

Below, we first introduce the weighting strategy for the HWENO-1.

1. Compute the nonlinear weights using Z-type weighting strategy in [2, 8] by

$$\omega_k = \frac{\bar{\omega}_k}{\sum_l \bar{\omega}_l} \quad \text{with} \quad \bar{\omega}_k = \gamma_k \left(1 + \frac{\tau}{\beta_k + \epsilon} \right) \quad k = 0, 1, 3, \quad (2.15)$$

where $\epsilon = 10^{-40}$ is set to avoid the denominator being zero. The linear weights, $\{\gamma_0, \gamma_1, \gamma_3\}$, are chosen as $\{0.6, 0.2, 0.2\}$ in this paper. We refer to [39, 42] for more details on linear and nonlinear weights.

2. Reconstruct the x -dimension first-order moment, \bar{v}_5^n , by

$$\tilde{v}_5^n = \frac{\omega_0}{\gamma_0} \left(\tilde{v}_{i,j,0}^n - \gamma_1 \tilde{v}_{i,j,1}^n - \gamma_3 \tilde{v}_{i,j,3}^n \right) + \omega_1 \tilde{v}_{i,j,1}^n + \omega_3 \tilde{v}_{i,j,3}^n. \quad (2.16)$$

The WENO weighting procedure presented in (2.16) originates from the WENO-ZQ reconstruction method, as detailed in [42], and has been further developed in [1, 38, 39]. For a detailed accuracy analysis, we refer readers to these studies. A similar formula will be employed later for reconstructing a polynomial in $I_{i,j}$.

The HWENO-2 reconstructs the first-order moment \bar{v}_5^n as follows.

1. Separate the discontinuities from broad-band smooth fluctuations as illustrated in [14, 15] and also motivated by the Z-type weighting strategy in [2, 8] by first taking

$$\eta_k = \left(1 + \frac{\tau}{\beta_k + \epsilon} \right)^6 \quad k = 1, 2, 3, \quad (2.17)$$

where $\epsilon = 10^{-40}$ is used to avoid the denominator being zero as in [2]. If there is no discontinuity involved, we can find that $\eta_k \approx 1$ for all k . If there is discontinuity involved for the global three-cells stencil, the η value for a smooth small stencil can be greatly enlarge with a magnitude of $O(\Delta x^{-12})$. Then, we normalize $\{\eta_k\}_{k=1}^3$ with

$$\kappa_k = \frac{\eta_k}{\sum_{l=1}^3 \eta_l} \quad k = 1, 2, 3. \quad (2.18)$$

2. Reconstruct the x -dimension first-order moment \bar{v}_5^n by:

$$\tilde{v}_5^n = \tilde{v}_{i,j,0}^n, \quad \text{if} \quad \min_k \kappa_k > C_T, \quad (2.19)$$

otherwise

$$\tilde{v}_5^n = \begin{cases} \tilde{v}_{i,j,1}^n, & \text{if } \kappa_1 > \kappa_3, \\ \tilde{v}_{i,j,3}^n, & \text{if } \kappa_3 > \kappa_1. \end{cases} \quad (2.20)$$

where C_T is a parameter deciding whether a corresponding polynomial should be involved [15]. We empirically choose $C_T = 10^{-3}$ as in [19]. For treating discontinuity, unlike [15, 19], we only choose the smoothest polynomial for reconstruction, since the weighted summation does not increase the order of accuracy for our case. When $\{\kappa_k\}$ matches the smoothness of the three-cells stencil, we directly use $\tilde{v}_{i,j,0}^n$ for optimal accuracy.

Remark 2.1 As outlined in the introduction, the reconstruction presented in (2.19) fundamentally aligns with the ENO or TENO type of reconstruction. For simplicity, we refer to this reconstruction as HWENO-2, rather than HENO or HTENO, considering it as a unique weighting strategy where the weights are either 0 or 1.

The first-order moment in y direction can be reconstructed in a similar way; we denote the reconstructed first-order moment in this direction by \tilde{w}_5^n .

Step 2. Recover the reconstructed $H^n(x, y)$ on $I_{i,j}$.

Step 2.1. Collect information from different 2-D polynomials.

1. Construct a polynomial $\tilde{q}_0(x, y) := \sum_{l=1}^{11} a_l^{q_0} P_l(x, y)$ such that

$$\begin{aligned} \frac{1}{\Delta x \Delta y} \iint_{I_s} \tilde{q}_0(x, y) dx dy &= \bar{u}_s^n, \quad s = 1, 2, \dots, 9, \\ \frac{1}{\Delta x \Delta y} \iint_{I_5} \tilde{q}_0(x, y) \left(\frac{x - x_i}{\Delta x} \right) dx dy &= \tilde{v}_5^n, \\ \frac{1}{\Delta x \Delta y} \iint_{I_5} \tilde{q}_0(x, y) \left(\frac{y - y_j}{\Delta y} \right) dx dy &= \tilde{w}_5^n. \end{aligned} \quad (2.21)$$

Let $q_0(x, y) = \sum_{l=1}^{10} a_l^{q_0} P_l(x, y)$, which is the orthogonal projection of $\tilde{q}_0(x, y)$ to $P^3(I_{i,j})$. We provide the explicit expressions of $\{a_l^{q_0}\}_{l=1}^{10}$ in Appendix A.

2. Construct four quadratic polynomial $\{q_k(x, y)\}_{k=1}^4 := \{\sum_{l=1}^6 a_l^{q_k} P_l(x, y)\}_{k=1}^4$ satisfying

$$\begin{aligned} \frac{1}{\Delta x \Delta y} \iint_{I_s} q_k(x, y) dx dy &= \bar{u}_s^n, \\ \frac{1}{\Delta x \Delta y} \iint_{I_5} q_k(x, y) \frac{x - x_i}{\Delta x} dx dy &= \tilde{v}_5^n, \\ \frac{1}{\Delta x \Delta y} \iint_{I_5} q_k(x, y) \frac{y - y_j}{\Delta y} dx dy &= \tilde{w}_5^n, \end{aligned} \quad (2.22)$$

where

$$\begin{aligned} s = 1, 2, 4, 5, & \text{ for } k = 1; \quad s = 2, 3, 5, 6, \text{ for } k = 2; \\ s = 4, 5, 7, 8, & \text{ for } k = 3; \quad s = 5, 6, 8, 9, \text{ for } k = 4. \end{aligned} \quad (2.23)$$

The explicit expressions of $\{a_l^{q_k}\}$ are given in Appendix A.

3. Compute the smoothness indicator [20, 23, 33] $\{\hat{\beta}_k\}_{k=0}^4$ of $\{q_k(x, y)\}_{k=0}^4$:

$$\begin{aligned} \hat{\beta}_0 &= \frac{1}{\Delta x \Delta y} \sum_{l_1+l_2 \leqslant 3} \iint_{I_{i,j}} \left(\Delta x^{l_1} \Delta y^{l_2} \frac{\partial^{|l_1+l_2|}}{\partial x^{l_1} \partial y^{l_2}} q_0(x, y) \right)^2 dx dy; \\ \hat{\beta}_k &= \frac{1}{\Delta x \Delta y} \sum_{l_1+l_2 \leqslant 2} \iint_{I_{i,j}} \left(\Delta x^{l_1} \Delta y^{l_2} \frac{\partial^{|l_1+l_2|}}{\partial x^{l_1} \partial y^{l_2}} q_k(x, y) \right)^2 dx dy, \quad k = 1, 2, 3, 4. \end{aligned} \quad (2.24)$$

The explicit expression of $\{\hat{\beta}_k\}_{k=0}^4$ can be given by

$$\begin{aligned} \hat{\beta}_0 &= \left(a_2^{q_0} + \frac{1}{10} a_7^{q_0} \right)^2 + \left(a_3^{q_0} + \frac{1}{10} a_{10}^{q_0} \right)^2 + \frac{13}{3} (a_4^{q_0})^2 + \frac{7}{6} (a_5^{q_0})^2 + \frac{13}{3} (a_6^{q_0})^2 \\ &\quad + \frac{781}{20} (a_7^{q_0})^2 + \frac{47}{10} (a_8^{q_0})^2 + \frac{47}{10} (a_9^{q_0})^2 + \frac{781}{20} (a_{10}^{q_0})^2; \\ \hat{\beta}_k &= (a_2^{q_k})^2 + (a_3^{q_k})^2 + \frac{13}{3} (a_4^{q_k})^2 + \frac{7}{6} (a_5^{q_k})^2 + \frac{13}{3} (a_6^{q_k})^2 \quad \text{for } k = 1, 2, 3, 4. \end{aligned} \quad (2.25)$$

4. Compute a full stencil global reference smoothness indicator:

$$\hat{\tau} = \left(\frac{|\hat{\beta}_0 - \hat{\beta}_1| + |\hat{\beta}_0 - \hat{\beta}_2| + |\hat{\beta}_0 - \hat{\beta}_3| + |\hat{\beta}_0 - \hat{\beta}_4|}{4} \right)^2. \quad (2.26)$$

Similarly, by the Taylor expansion, we can easily check that $\hat{\tau} = O(\Delta x^6)$, if there is no discontinuity involved.

Step 2.2. Weight the collected 2-D polynomials.

The HWENO-1 weights the polynomials as follows.

1. Compute the nonlinear weights using Z-type weighting strategy in [2, 8] by

$$\hat{\omega}_k = \frac{\tilde{\omega}_k}{\sum_l \tilde{\omega}_l} \quad \text{with } \tilde{\omega}_k = \gamma_k \left(1 + \frac{\tau}{\beta_k + \epsilon} \right) \quad k = 0, 1, 2, 3, 4, \quad (2.27)$$

where $\epsilon = 10^{-40}$ is set to avoid the denominator being zero. The linear weights, $\{\gamma_k\}_{k=0}^4$ are chosen as $\{0.6, 0.1, 0.1, 0.1, 0.1\}$ in this paper.

2. Construct $H^{(i,j)}(x, y) := \sum_{l=1}^{10} a_l P_l(x, y)$:

$$H^{(i,j)}(x, y) = \frac{\hat{\omega}_0}{\hat{\gamma}_0} \left(q_0(x, y) - \sum_{k=1}^4 \hat{\gamma}_k q_k(x, y) \right) + \sum_{k=1}^4 \hat{\omega}_k q_k(x, y), \quad (x, y) \in I_{i,j}. \quad (2.28)$$

Here, the coefficients $\{a_l\}$ can be explicitly given by

$$\begin{aligned} a_1 &= \bar{u}_5^n; \quad a_2 = 12\bar{v}_5^n; \quad a_3 = 12\bar{w}_5^n; \\ a_l &= \frac{\hat{\omega}_0}{\hat{\gamma}_0} a_l^{q_0} + \sum_{k=1}^4 \left(\hat{\omega}_k - \frac{\hat{\omega}_0}{\hat{\gamma}_0} \hat{\gamma}_k \right) a_l^{q_k} \quad \text{for } l = 4, 5, 6; \\ a_l &= \frac{\hat{\omega}_0}{\hat{\gamma}_0} a_l^{q_0} \quad \text{for } l = 7, 8, \dots, 10. \end{aligned} \quad (2.29)$$

The HWENO-2 weights the polynomials as follows.

1. Compute the separation parameters $\{\hat{\eta}_k\}_{k=1}^4$ and the corresponding normalized parameters $\{\hat{k}_k\}_{k=1}^4$ similarly:

$$\hat{k}_k = \frac{\hat{\eta}_k}{\sum_{l=1}^3 \hat{\eta}_l} \quad \text{with } \hat{\eta}_k = \left(1 + \frac{\hat{\tau}_6}{\hat{\beta}_k + \epsilon} \right)^6 \quad \text{for } k = 1, 2, 3, 4, \quad (2.30)$$

where $\epsilon = 10^{-40}$.

2. Construct $H^{(i,j)}(x, y)$ by

$$H^{(i,j)}(x, y) = q_0(x, y), \quad \text{if } \min_k \hat{k}_k > C_T, \quad (2.31)$$

otherwise

$$H^{(i,j)}(x, y) = q_K(x, y) \quad \text{with } K \text{ being the index such that } \hat{k}_K = \max_k \hat{k}_k. \quad (2.32)$$

Here, C_T is chosen as 10^{-3} .

In particular, if $\bar{v}_{i,j}^n = \bar{v}_{i,j,0}^n$, $\bar{w}_{i,j}^n = \bar{w}_{i,j,0}^n$ (with similar notation), and $H^{(i,j)}(x, y) = q_0(x, y) \quad \forall i, j$, we call such a reconstruction linear reconstruction.

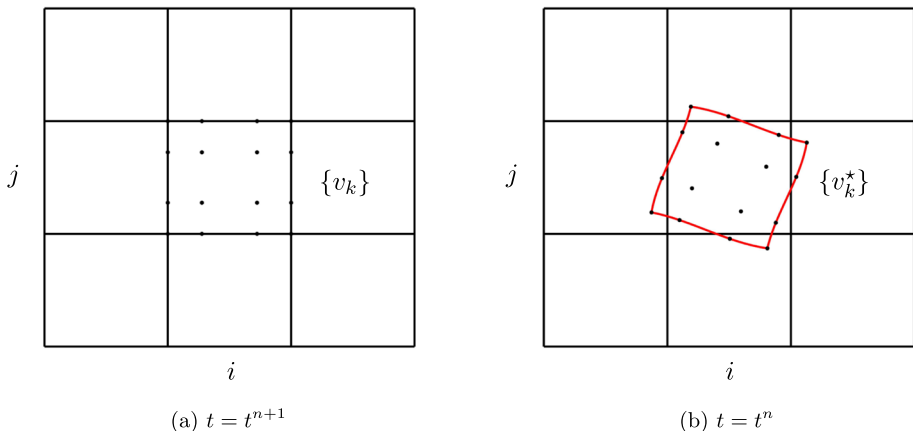


Fig. 3 Schematic illustration for the GLL points $\{v_k\}$ at t^{n+1} time level (a) and for the characteristic feet $\{v_k^*\}$ at t^n time level (b). Left: the black solid lines represent the Eulerian mesh; the black dots are the GLL points located on the Eulerian cell $I_{i,j}$. Right: the black solid lines represent the Eulerian mesh; the red solid lines represent the boundary of $\tilde{I}_{i,j}^*$; the black dots are the characteristic feet obtained by solving (2.2)

2.2 Constructing Cubic-Curved Upstream Cells and Approximating $w(x, y, t^n)$

To evaluate the right-hand side of (2.5), it remains to provide the approximations of $\{I_{i,j}^*\}$ and $w(x, y, t^n)$. For a given index (i, j) , the cubic-curved quadrilateral upstream cell, $\tilde{I}_{i,j}^*$, and the cubic polynomial $\tilde{w}(x, y)$ on $\tilde{I}_{i,j}^*$ are constructed by the following procedure.

Step 1. Tracing characteristics backward in time.

We locate 4×4 Gauss-Legendre-Lobatto (GLL) points, denoted by $\{v_k\}$, on $I_{i,j}$. We determine the characteristic feet, denoted by $\{v_k^*\}$, of these GLL points by solving (2.2) at $t = t^n$ (see Fig. 3). In practice, we solve the ODEs (2.2) by a fourth-order Runge–Kutta (RK) method.

Step 2. Constructing cubic-curved quadrilateral upstream cell $\tilde{I}_{i,j}^*$.

We determine the cubic-curved quadrilateral $\tilde{I}_{i,j}^*$ by constructing its edges. The edges of the cubic-curved quadrilateral upstream cells are constructed by a cubic interpolation procedure (see [41]). In particular, we prefer to use a parametric form to present any cubic-curved edge:

$$\begin{cases} x(\xi) = x_a\xi^3 + x_b\xi^2 + x_c\xi + x_d, \\ y(\xi) = y_a\xi^3 + y_b\xi^2 + y_c\xi + y_d, \end{cases} \quad \xi \in [-1, 1]. \quad (2.33)$$

Step 3. Constructing $\tilde{w}(x, y)$.

By the adjoint problem (2.3), we have

$$w(x(v_k^*), y(v_k^*)) = W(x(v_k), y(v_k)) \quad \text{for } k = 1, 2, \dots, 16. \quad (2.34)$$

Hence, by a standard least square procedure, we obtain a cubic polynomial $\tilde{w}(x, y) \in P^3$ such that $w(x, y, t^n) - \tilde{w}(x, y) = O(\Delta x^4)$.

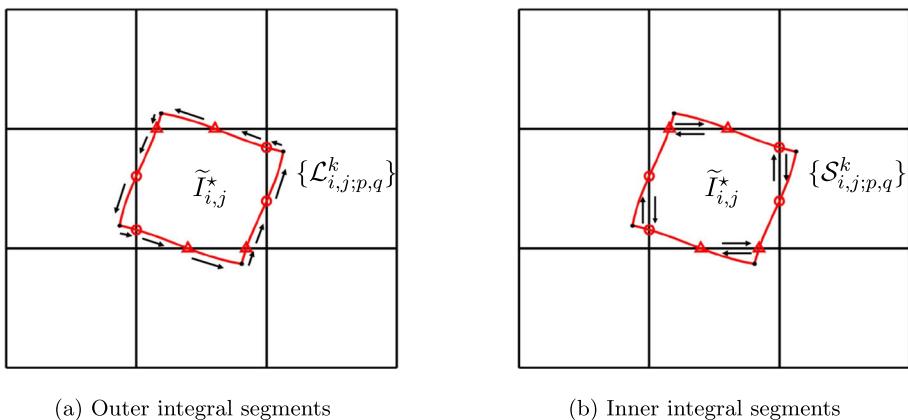


Fig. 4 Schematic illustration for the outer integral segments (a) and the inner integral segments (b). The red circles and triangles are the intersections of $\tilde{I}_{i,j}^*$ and the Eulerian mesh

2.3 Numerical Integration

For numerically evaluating the right-hand side of (2.5), we integrate the piecewise polynomial $H^n(x, y)\tilde{w}(x, y)$ over each $\tilde{I}_{i,j}^*$, which may cross different Eulerian background cells. Hence, $\tilde{I}_{i,j}^*$ is first clipped into curved polygons such that $\tilde{I}_{i,j}^* = \cup_{(p,q)}(\tilde{I}_{i,j}^* \cap I_{p,q})$ and the integrand is smooth in each polygon. For conciseness, the curved polygons $\{\tilde{I}_{i,j}^* \cap I_{p,q}\}$ are denoted by $\{\tilde{I}_{i,j;p,q}^*\}$. In particular, we are concerned about the information along the edges of $\{\tilde{I}_{i,j;p,q}^*\}$. The edges of $\{\tilde{I}_{i,j;p,q}^*\}$, overlapping $\partial\tilde{I}_{i,j}^*$, with counterclockwise direction with respect to $\tilde{I}_{i,j}^*$ are denoted by $\{\mathcal{L}_{i,j;p,q}^k\}$ (see Fig. 4a). We call $\{\mathcal{L}_{i,j;p,q}^k\}$ the *outer integral segments* of the upstream cell $\tilde{I}_{i,j}^*$. Similarly, the edges of $\{\tilde{I}_{i,j;p,q}^*\}$, overlapping mesh lines, with counterclockwise direction with respect to the corresponding curved polygons are denoted by $\{\mathcal{S}_{i,j;p,q}^k\}$ (see Fig. 4b). We call $\{\mathcal{S}_{i,j;p,q}^k\}$ the *inner integral segments* of $\tilde{I}_{i,j}^*$. We call the procedure of determining the integral segments the clipping method. For implementation, we refer to [41] for more details.

With the clipped outer integral segments, $\{\mathcal{L}_{i,j;p,q}^k\}$, as well as the inner integral segments, $\{\mathcal{S}_{i,j;p,q}^k\}$, we evaluate the right-hand side of (2.5) as follows

$$\begin{aligned} \frac{1}{\Delta x \Delta y} \iint_{I_{i,j}^*} u(x, y, t^n) w(x, y) dx dy &\approx \frac{1}{\Delta x \Delta y} \iint_{\tilde{I}_{i,j}^*} H^n(x, y) \tilde{w}(x, y) dx dy \\ &= \frac{1}{\Delta x \Delta y} \sum_{(p,q)} \iint_{\tilde{I}_{i,j;p,q}^*} H^{(p,q)}(x, y) \tilde{w}(x, y) dx dy \\ &= \frac{1}{\Delta x \Delta y} \sum_{(p,q)} \int_{\partial(\tilde{I}_{i,j;p,q}^*)} [Pdx + Qdy] \end{aligned}$$

$$= \frac{1}{\Delta x \Delta y} \sum_{(p,q)} \left\{ \sum_k \int_{\mathcal{L}_{i,j;p,q}^k} [Pdx + Qdy] \right. \\ \left. + \sum_k \int_{S_{i,j;p,q}^k} [Pdx + Qdy] \right\}, \quad (2.35)$$

where $P(x, y)$ and $Q(x, y)$ are piecewise smooth auxiliary functions such that

$$-\frac{\partial P}{\partial y} + \frac{\partial Q}{\partial x} = H^{(p,q)}(x, y)\tilde{w}(x, y). \quad (2.36)$$

It is straightforward for evaluating the line integral on $\{S_{i,j;p,q}^k\}$. For the integral on an outer integral segment, say $\mathcal{L}_{i,j;p,q}^k$,

$$\int_{\mathcal{L}_{i,j;p,q}^k} [Pdx + Qdy] = \int_{\xi_k}^{\xi_{k+1}} \left[P(x(\xi), y(\xi)) x'(\xi) + Q(x(\xi), y(\xi)) v'_q(\xi) \right] d\xi, \quad (2.37)$$

where ξ_k and ξ_{k+1} represent the ξ value of the start point and end point of $\mathcal{L}_{i,j;p,q}^k$ (2.33).

The proposed SL HWENO schemes also equip a PP limiter [37], when the analytical solution of (2.1) stays positive. For the implementation of this PP limiter, we refer to [41] for a detailed description.

Remark 2.2 We can numerically prove that the numerical update provided by (2.35) is unconditionally stable for linear transport equations with constant coefficients and periodic boundary condition if $H^n(x, y)$ is reconstructed by the linear reconstruction defined in Sect. 2.1. The proof is accomplished by the von Neumann analysis. We arrange this proof in Appendix B.

3 SL HWENO Schemes for Nonlinear Models

The non-splitting SL HWENO schemes are coupled with a fourth-order RKEI in the same framework as in [3] to solve nonlinear models such as the Vlasov–Poisson system, the guiding center Vlasov model, and the incompressible Euler equations in the vorticity-stream function formulation. Below, we briefly describe these three models.

Arising from collisionless plasma, the Vlasov–Poisson system reads

$$f_t + vf_x + E(x, t)f_v = 0, \quad (3.1)$$

$$E(x, t) = -\phi_x, \quad -\phi_{xx}(x, t) = \rho(x, t), \quad (3.2)$$

where x represents the spatial position, v is the velocity, $f(x, v, t)$ is the probability distribution function describing the probability of a particle at position x with velocity v at time t . The electric field E is determined by the Poisson's Eq. (3.2). ϕ is the self-consistent electrostatic potential. $\rho = \int_{\mathbb{R}} f(x, v, t)dv - \rho_0$ is the charge density with $\rho_0 = \frac{1}{|\Omega_x|} \int_{\Omega_x} \int_{\mathbb{R}} f(x, v, 0)dv dx$.

The 2-D guiding center Vlasov model describes highly magnetized plasma in the transverse plane of a tokamak [13, 36], which can be written as:

$$\rho_t + \nabla \cdot (\mathbf{E}^\perp \rho) = 0, \quad (3.3)$$

$$-\Delta \Phi = \rho, \quad \mathbf{E}^\perp = (-\Phi_y, \Phi_x), \quad (3.4)$$

where $\rho(x, y, t)$ is the charge density and \mathbf{E} is the electric field depends on ρ via the Poisson's Eq. (3.4).

The 2-D incompressible Euler equations in vorticity-stream function formulation reads

$$\omega_t + \nabla \cdot (\mathbf{u}\omega) = 0, \quad (3.5)$$

$$\Delta\psi = \omega, \quad \mathbf{u} = (-\psi_y, \psi_x), \quad (3.6)$$

where $\omega(x, y, t)$ is the vorticity of the fluid, $\mathbf{u} := (u_1, u_2)$ is the velocity field, and ψ is the stream-function determined by the Poisson Eq. (3.6).

Notice that these three models can be written in the form of

$$u_t + \nabla \cdot (\mathbf{V}(u(\mathbf{x}, t))u) = 0, \quad (3.7)$$

where $\mathbf{V}(u(\mathbf{x}, t))$ represents the velocity field. We briefly summarize the SL HWENO scheme coupled with the fourth-order RKEI as follows.

$$\begin{aligned} \bar{u}^{(1)} &= \bar{u}^n \\ \bar{u}^{(2)} &= SLHWENO \left(\frac{1}{2} \mathbf{V}(\bar{u}^{(1)}), \Delta t \right) \bar{u}^n \\ \bar{u}^{(3)} &= SLHWENO \left(\frac{1}{2} \mathbf{V}(\bar{u}^{(2)}), \Delta t \right) \bar{u}^n \\ \bar{u}^{(4)} &= SLHWENO \left(-\frac{1}{2} \mathbf{V}(\bar{u}^{(1)}) + \mathbf{V}(\bar{u}^{(3)}), \Delta t \right) \bar{u}^{(2)} \\ \bar{u}^{n+1} &= SLHWENO \left(-\frac{1}{12} \mathbf{V}(\bar{u}^{(1)}) + \frac{1}{6} \mathbf{V}(\bar{u}^{(2)}) + \frac{1}{6} \mathbf{V}(\bar{u}^{(3)}) + \frac{1}{4} \mathbf{V}(\bar{u}^{(4)}), \Delta t \right) \\ &\quad SLHWENO \left(\frac{1}{4} \mathbf{V}(\bar{u}^{(1)}) + \frac{1}{6} \mathbf{V}(\bar{u}^{(2)}) + \frac{1}{6} \mathbf{V}(\bar{u}^{(3)}) - \frac{1}{12} \mathbf{V}(\bar{u}^{(4)}), \Delta t \right) \bar{u}^n, \end{aligned} \quad (3.8)$$

where $SLHWENO(\mathbf{V}(\bar{u}^{(k)}), \frac{1}{2}\Delta t)\bar{u}^{(l)}$ represents the solution evolved from $\bar{u}^{(l)}$ with time step $\frac{1}{2}\Delta t$ and velocity field $\mathbf{V}(\bar{u}^{(k)})$ by a non-splitting SL HWENO scheme. For approximating the velocity field, we use the Fast Fourier transform to solve the Poisson's equations.

4 Numerical Tests

4.1 Linear Transport Equations

In this subsection, we test two benchmark problems: the transport equation with constant coefficients and the swirling deformation flow. We apply four numerical schemes, denoted as SL HWENO-1, SL HWENO-2, SL HWENO-3, and SL WENO-ZQ schemes. The first two are newly developed schemes presented in this paper. The third scheme is essentially the same as the SL HWENO scheme described here, but with the HWENO-1 or HWENO-2 reconstruction replaced by the HWENO-3 reconstruction from [39]. In the HWENO-3 reconstruction, we substitute the $p_0(x, y) \in P^4$ in [39] with the $q_0(x, y)$ constructed in Sect. 2.1, aiming to maintain fourth-order spatial accuracy and enable the application of the PP limiter. This adjustment is necessary as we currently can only ensure the PP property for piecewise P^3 polynomials in space. The SL WENO-ZQ scheme is identical to the non-splitting SL scheme found in [41].

A brief discussion on computational efficiency is pertinent here. While efficiency is not the central focus of this paper, it is important to note that the proposed SL schemes demonstrate significant improvements in computational time, especially when compared to traditional Eulerian schemes. Our SL schemes are capable of operating with arbitrary large CFL numbers, which allows for larger time steps and thus enhanced efficiency. In contrast, Eulerian schemes (e.g., finite volume RK WENO or HWENO schemes) typically operate with a CFL number around 0.6, marking a substantial difference in time-stepping capabilities. However, due to the extensive scope required for a rigorous comparison with Eulerian schemes, such an analysis is beyond the scope of the current revision. Nonetheless, the tests in this section include comparisons of L^1 and L^∞ errors against CPU times for all four SL schemes, providing a quantitative measure of their efficiency.

Through the following tests, our goal is to showcase the performance of the SL schemes and compare the differences between various reconstructions in terms of spatial and temporal accuracy, numerical stability, and resolution of complex solution structures.

Unless otherwise specified, we set $\Delta t = \frac{\text{CFL}}{\max_{\Delta x} |a(x, y, t)| + \max_{\Delta y} |b(x, y, t)|}$ with $\text{CFL} = 10.2$. Here, $\text{CFL} = 10.2$ is chosen to avoid the situation where the SL schemes decay into simple shifting of numerical solutions for the transport equation with constant coefficients. The PP limiter is applied to problems with non-negative initial conditions.

Example 4.1 (Transport equation with constant coefficients). Consider

$$u_t + u_x + u_y = 0, \quad x \in [-\pi, \pi], \quad y \in [-\pi, \pi], \quad (4.1)$$

with a smooth initial condition, $u(x, y, 0) = \sin(10(x + y))$, and the periodic boundary condition. The exact solution for this problem is $u(x, y, t) = \sin(10(x + y - 2t))$. In Table 1, we present the L^1 errors, L^∞ errors, and their corresponding spatial orders of accuracy for the SL schemes. As indicated, all schemes achieve fourth-order convergence. However, the SL HWENO-3 and SL WENO-ZQ schemes require denser meshes to reach fourth-order accuracy. In Fig. 5, we display log-log plots of CPU times versus the L^1 and L^∞ errors under the same conditions as in Table 1. These plots reveal that the SL HWENO-1 and SL HWENO-2 schemes are more efficient. Lastly, Fig. 6 shows the cross-sections of the numerical solutions at $x = y$ for the SL schemes at $T = 20$, using a fixed mesh size of 80×80 . At this resolution, with four points per wavelength at $x = y$, the SL HWENO-3 and SL WENO-ZQ schemes appear to produce more smearing compared to the other two schemes.

Example 4.2 (Swirling deformation flow). Consider

$$u_t - \left(2\pi \cos^2\left(\frac{x}{2}\right) \sin(y) g(t) u\right)_x + \left(2\pi \sin(x) \cos^2\left(\frac{y}{2}\right) g(t) u\right)_y = 0, \quad (4.2)$$

$$x \in [-\pi, \pi], \quad y \in [-\pi, \pi],$$

where $g(t) = \cos(\pi t / T)$ with $T = 1.5$. We consider (4.2) with the following smooth initial condition

$$u(x, y, 0) = \begin{cases} r_0^b \cos\left(\frac{r^b(\mathbf{x})\pi}{2r_0^b}\right)^6 & \text{if } r^b(\mathbf{x}) < r_0^b, \\ 0, & \text{otherwise,} \end{cases} \quad (4.3)$$

where $r_0^b = 0.3\pi$, $r^b(\mathbf{x}) = \sqrt{(x - x_0^b)^2 + (y - y_0^b)^2}$ and the center of the cosine bell $(x_0^b, y_0^b) = (0.3\pi, 0)$. Zero boundary condition is equipped for this test. In Table 2, we

Table 1 (Transport equation with constant coefficients). L^1 errors, L^∞ errors and corresponding spatial orders of accuracy for the SL schemes applied to Eq.(4.1) with initial condition $u(x, y, 0) = \sin(10(x + y))$, evaluated at $T = 20$ with CFL = 10.2

mesh	SL HWENO-1				SL HWENO-2			
	L^1 error	order	L^∞ error	order	L^1 error	order	L^∞ error	order
20 × 20	6.40E-01	–	9.97E-01	–	6.40E-01	–	1.05E+00	–
40 × 40	2.19E-01	1.55	5.79E-01	0.78	2.12E-01	1.59	3.95E-01	1.40
80 × 80	1.47E-02	3.90	3.85E-02	3.91	1.48E-02	3.84	3.93E-02	3.33
160 × 160	1.00E-03	3.88	2.42E-03	3.99	1.00E-03	3.89	2.42E-03	4.02
320 × 320	6.31E-05	3.98	1.46E-04	4.06	6.31E-05	3.98	1.46E-04	4.06
SL HWENO-3				SL WENO-ZQ				
20 × 20	6.40E-01	–	9.96E-01	–	6.40E-01	–	9.96E-01	–
40 × 40	6.31E-01	0.02	1.00E+00	-0.01	6.13E-01	0.06	9.66E-01	0.05
80 × 80	1.32E-01	2.26	2.89E-01	1.80	1.99E-01	1.62	3.74E-01	1.37
160 × 160	1.40E-03	6.55	3.76E-03	6.27	1.66E-02	3.58	4.21E-02	3.15
320 × 320	6.58E-05	4.41	1.68E-04	4.48	3.10E-04	5.75	1.26E-03	5.07

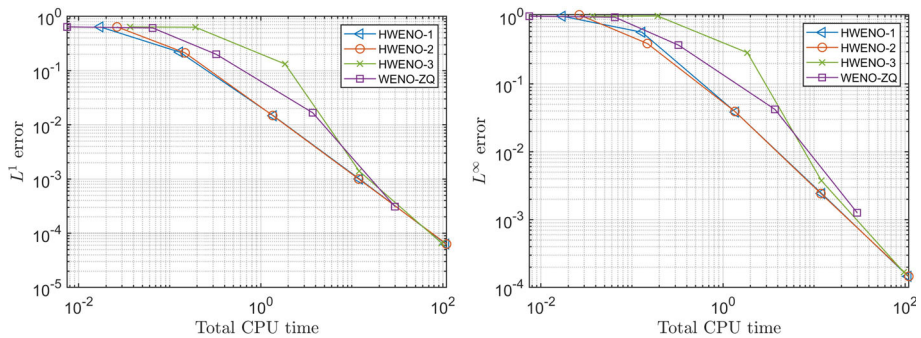


Fig. 5 (Transport equation with constant coefficients). Log-log plots comparing CPU times and errors for the SL schemes: L^1 errors (left) and L^∞ errors (right), under the same settings as in Table 1

present the L^1 errors, L^∞ errors and the corresponding spatial orders of accuracy of the SL schemes. As illustrated, it is more evident that the SL HWENO-1 and SL HWENO-2 schemes achieve fourth-order accuracy. However, due to numerical dissipation, it is harder to demonstrate fourth-order spatial accuracy for the SL HWENO-2 and SL WENO-ZQ schemes. In Fig. 7, we present log-log plots of CPU times versus the L^1 and L^∞ errors, using the same conditions as in Table 2. Among these, the SL HWENO-3 scheme exhibits the least efficient performance for both L^1 and L^∞ errors. In terms of the L^1 error, the SL WENO-ZQ scheme proves to be the most efficient. However, for the L^∞ error, the performance of the SL WENO-ZQ scheme is nearly as poor as that of the SL HWENO-3 scheme.

In Fig. 8, we demonstrate the temporal order of accuracy for the SL schemes by maintaining a fixed spatial mesh while varying the CFL number. We observe that the temporal order reaches fifth-order for the swirling deformation flow, which is unexpectedly one order higher than the anticipated fourth-order. However, we emphasize that this is not a general phenomenon. It is possible that this unique outcome is due to the specific symmetry inherent

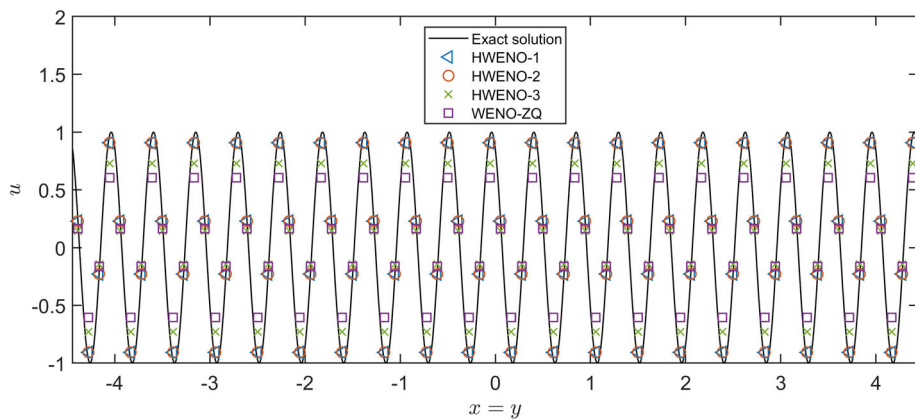


Fig. 6 (Transport equation with constant coefficients). Cross-sections of the numerical solutions obtained using the SL schemes for Eq. (4.1) with initial condition $u(x, y, 0) = \sin(x + y)$. These solutions correspond to $T = 20$ and are based on a 100×100 mesh with $\text{CFL} = 10.2$

Table 2 (Swirling deformation flow). L^1 errors, L^∞ errors and corresponding spatial orders of accuracy for the SL schemes applied to Eq. (4.2) with initial condition (4.3), evaluated at $t = 1.5$ with $\text{CFL} = 10.2$

mesh	SL HWENO-1				SL HWENO-2			
	L^1 error	order	L^∞ error	order	L^1 error	order	L^∞ error	order
20×20	2.42E-03	–	2.80E-01	–	2.48E-03	–	2.82E-01	–
40×40	1.72E-04	3.82	2.06E-02	3.77	2.97E-04	3.06	2.84E-02	3.31
80×80	2.06E-05	3.05	2.33E-03	3.14	4.23E-05	2.81	7.72E-03	1.88
160×160	8.61E-07	4.58	9.72E-05	4.58	3.10E-06	3.77	7.95E-04	3.28
320×320	3.67E-08	4.55	4.10E-06	4.57	1.39E-07	4.49	5.42E-05	3.87
640×640	1.50E-09	4.62	1.95E-07	4.39	4.71E-09	4.88	3.06E-06	4.15
1280×1280	6.70E-11	4.48	1.08E-08	4.17	6.70E-11	6.13	1.08E-08	8.14
2560×2560	3.50E-12	4.26	6.60E-10	4.03	3.50E-12	4.26	6.60E-10	4.03
SL HWENO-3					SL WENO-ZQ			
20×20	4.21E-03	–	5.65E-01	–	3.97E-03	–	5.17E-01	–
40×40	8.45E-04	2.32	2.14E-01	1.40	7.67E-04	2.37	1.88E-01	1.46
80×80	6.54E-05	3.69	4.01E-02	2.41	6.26E-05	3.62	4.03E-02	2.22
160×160	3.93E-06	4.05	5.79E-03	2.79	2.96E-06	4.40	1.17E-02	1.78
320×320	3.47E-07	3.51	1.16E-03	2.32	1.12E-07	4.73	2.06E-03	2.50
640×640	1.94E-08	4.16	1.51E-04	2.94	3.98E-09	4.81	4.05E-04	2.35
1280×1280	2.07E-10	6.55	2.29E-06	6.04	1.38E-10	4.85	5.01E-05	3.02
2560×2560	3.62E-12	5.84	4.86E-09	8.88	4.18E-12	5.04	6.29E-08	9.64

in the swirling deformation flow. In this context, we merely report this observation without conducting a rigorous analysis. From Fig. 13, we can also observe that the SL HWENO-3 and SL WENO-ZQ schemes are less accurate for different CFL numbers, which also reflects the advantage of the proposed two new HWENO reconstructions. Another interesting phenomenon is that, before the temporal errors start to dominate, the errors decrease as the CFL

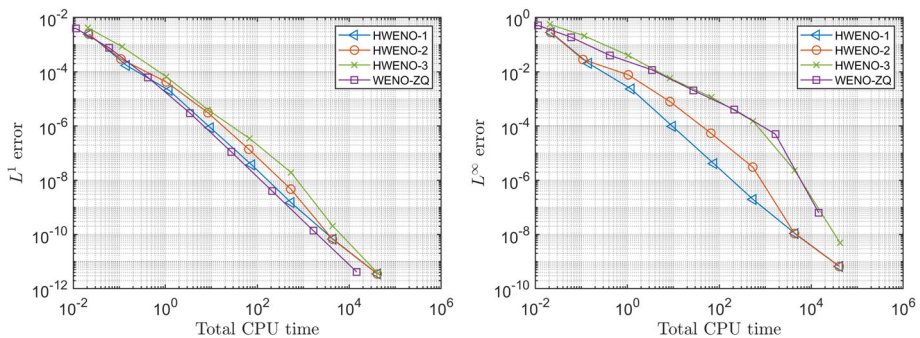


Fig. 7 (Swirling deformation flow). Log-log plots comparing CPU times and errors for the SL schemes: L^1 errors (left) and L^∞ errors (right), under the same settings as in Table 2

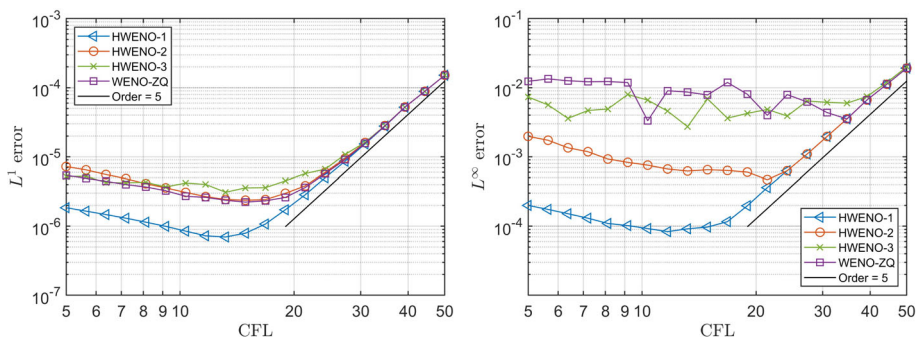


Fig. 8 (Swirling deformation flow). Temporal order of accuracy for the SL schemes, evaluated using L^1 error (left) and L^∞ error (right). The simulations use a fix mesh of 160×160 and calculate the errors at $t = 1.5$

number increases. This phenomenon is due to the accumulated spatial error, as simulations with smaller CFL numbers require more time steps.

To investigate the performance of the SL schemes with discontinuous solutions, we test Eq. (4.2) using the initial condition depicted in Fig. 9. The contour plots of the numerical solutions by the SL schemes at $t = 1.5$ are shown in Fig. 10, utilizing a mesh size of 100×100 and a CFL of 10.2. In Fig. 11, two cross-sections of the numerical solutions from Fig. 10 are presented. As observed, the SL schemes effectively capture the geometry of the solution. The SL HWENO-1 and SL HWENO-2 schemes demonstrate superior resolution while concurrently controlling numerical oscillations. In contrast, the SL HWENO-3 scheme exhibits more dissipation compared to the other schemes.

4.2 Nonlinear Vlasov–Poisson System

In this subsection, we test one benchmark test, the strong Landau damping, for Vlasov–Poisson system. Unless specified, we set $N_x = 128$, $N_v = 256$, CFL = 10.2, $\Delta t = \frac{\text{CFL}}{v_{\max}/\Delta x + \max\{|E|/\Delta v|}$ with v_{\max} representing the positive boundary in v -direction. The PP limiter is equipped for all tests.

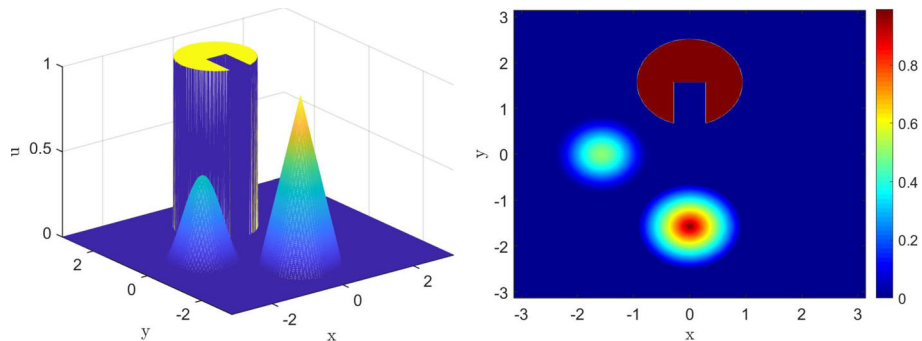


Fig. 9 (Swirling deformation flow). The mesh plot (left) and the contour plot (right) of the discontinuous initial data for (4.2)

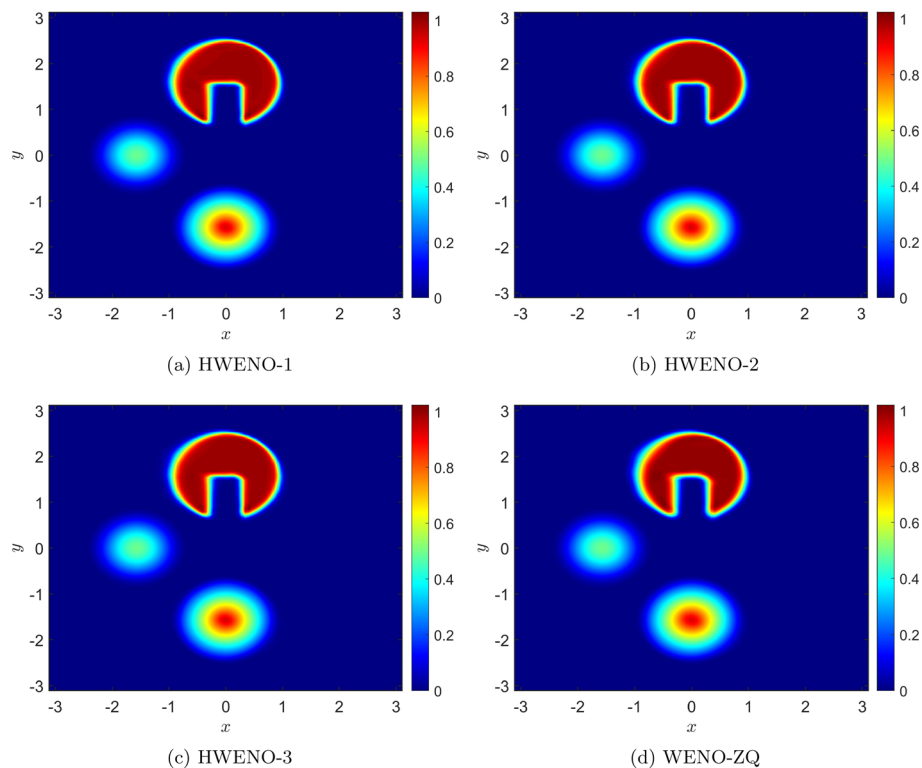


Fig. 10 (Swirling deformation flow). Contour plots of the numerical solutions obtained using the SL schemes for Eq. (4.2) with the initial condition shown in Fig. 9. These plots correspond to $t = 1.5$ and are based on a 100×100 mesh with $\text{CFL} = 10.2$

Example 4.3 (Strong Landau damping). Consider the VP system with the initial condition

$$f(x, v, t=0) = \frac{1}{\sqrt{2\pi}} (1 + \alpha \cos(kx)) \exp\left(-\frac{v^2}{2}\right), \quad x \in [0, 4\pi], \quad v \in [-2\pi, 2\pi], \quad (4.4)$$

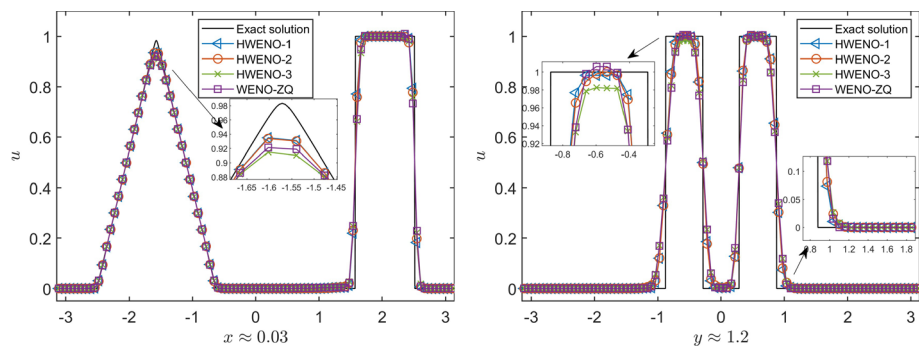


Fig. 11 (Swirling deformation flow). Cross-sections of the numerical solutions in Fig. 10 at $x \approx 0.03$ (left) and $y \approx 1.2$

Table 3 (Strong Landau damping). L^1 errors, L^∞ errors and corresponding spatial orders of accuracy for the SL schemes applied to the strong Landau damping problem, evaluated at $T = 5$ with CFL = 10.2

mesh	SL HWENO-1				SL HWENO-2			
	L^1 error	order	L^∞ error	order	L^1 error	order	L^∞ error	order
16 × 16	1.85E-02	—	2.39E-01	—	1.91E-02	—	2.56E-01	—
32 × 32	2.53E-03	2.87	6.12E-02	1.96	3.08E-03	2.63	8.63E-02	1.57
64 × 64	2.66E-04	3.25	5.96E-03	3.36	3.05E-04	3.33	1.86E-02	2.21
128 × 128	1.52E-05	4.13	4.78E-04	3.64	1.64E-05	4.22	5.32E-04	5.13
256 × 256	9.05E-07	4.07	3.18E-05	3.91	9.05E-07	4.18	3.18E-05	4.06
SL HWENO-3				SL WENO-ZQ				
16 × 16	2.56E-02	—	2.63E-01	—	2.37E-02	—	2.22E-01	—
32 × 32	7.95E-03	1.68	1.65E-01	0.67	6.18E-03	1.94	1.43E-01	0.63
64 × 64	7.39E-04	3.43	6.13E-02	1.43	7.16E-04	3.11	3.98E-02	1.85
128 × 128	1.53E-05	5.60	7.44E-04	6.36	3.51E-05	4.35	1.50E-02	1.40
256 × 256	9.04E-07	4.08	3.19E-05	4.54	1.17E-06	4.91	4.48E-05	8.39

where $k = 0.5$, $\alpha = 0.5$. In Table 3, we present the L^1 and L^∞ errors, along with the corresponding spatial orders of accuracy, for the SL schemes. These errors are calculated by comparing the solution with a reference solution obtained through mesh refinement. We note a distinct fourth-order accuracy for the SL HWENO-1 scheme. The SL HWENO-2 scheme shows a performance slightly inferior to that of the SL HWENO-1 scheme, but it is more accurate than both the SL HWENO-3 and SL WENO-ZQ schemes. Figure 12 features log-log plots of CPU times versus L^1 and L^∞ errors under the same settings in Table 3, providing a comparison of efficiency. Both the SL HWENO-1 and SL HWENO-2 schemes demonstrate greater efficiency in terms of both L^1 and L^∞ errors. In Fig. 13, we present the temporal order of accuracy of the SL schemes by fixing the spatial mesh while varying the CFL number. We observe approximately 3.8th-order temporal accuracy for the L^1 error and approximately 3.5th-order temporal accuracy for the L^∞ norm. Due to strong dissipation, the SL WENO-ZQ scheme exhibits much large L^∞ errors when its spatial errors dominate the total errors.

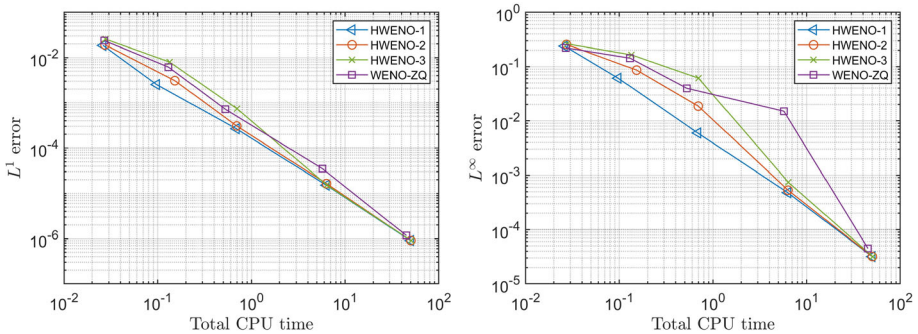


Fig. 12 (Strong Landau damping). Log-log plots comparing CPU times and errors for the SL schemes: L^1 errors (left) and L^∞ errors (right), under the same settings as in Table 3

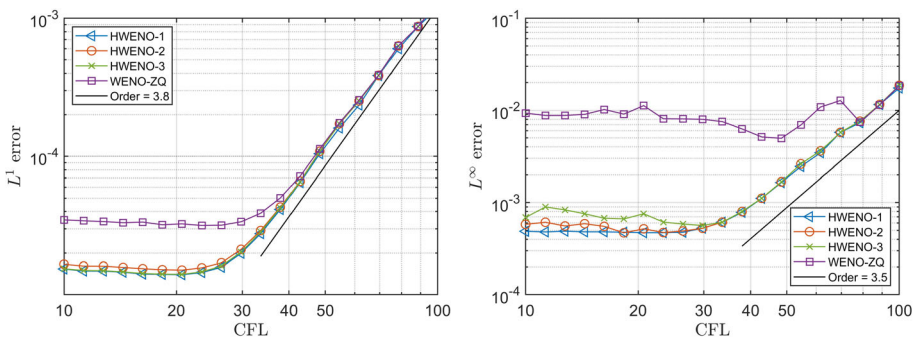


Fig. 13 (Strong Landau damping). Temporal order of accuracy for the SL schemes, evaluated using L^1 error (left) and L^∞ error (right). The simulations use a fix mesh of 128×128 and calculate the errors at $T = 5$

Figure 14 illustrates the time evolution of the first three Fourier modes of the electric field using the SL schemes, represented as $|E_k(0.5, t)|$, $|E_k(1.0, t)|$, and $|E_k(1.5, t)|$, following the notation in [25]. As observed, both the decaying and growing patterns of these three modes align with the numerical results reported in the literature. Additionally, the corresponding decay rates and growth rates presented in Fig. 14 closely match those found in previous studies, specifically in [21] and [25].

In Fig. 15, we display contour plots of the numerical solutions obtained using the SL schemes at $T = 40$. Additionally, cross-sections of these numerical solutions at $x \approx 2.6$, as depicted in Fig. 15, are shown in Fig. 16. We note that the numerical solutions effectively retains the filamentation structure of the strong Landau damping problem. From the color bars in Fig. 15 and the cross-sections, it is evident that the SL HWENO-3 and SL WENO-ZQ schemes tend to smear information at points with large gradients.

The VP system is characterized by several conserved quantities, including mass, L^p norms, energy, and entropy, as highlighted in [31]. In Fig. 17, we employ the SL HWENO-1 scheme to simulate strong Landau damping and assess the time evolution of the relative deviation of mass and L^1 norm in the numerical solution. To mitigate the effects of boundary truncation in the v dimension, we set $v_{\max} = 10$ for this simulation. The relative deviations in mass and L^1 norm are observed to be at the $O(10^{-12})$ level. Notably, the relative deviation of mass and L^1 norm coincides at every data point, underscoring the effectiveness of the PP limiter. Regarding the L^2 norm, energy, and entropy, the time evolution of their relative

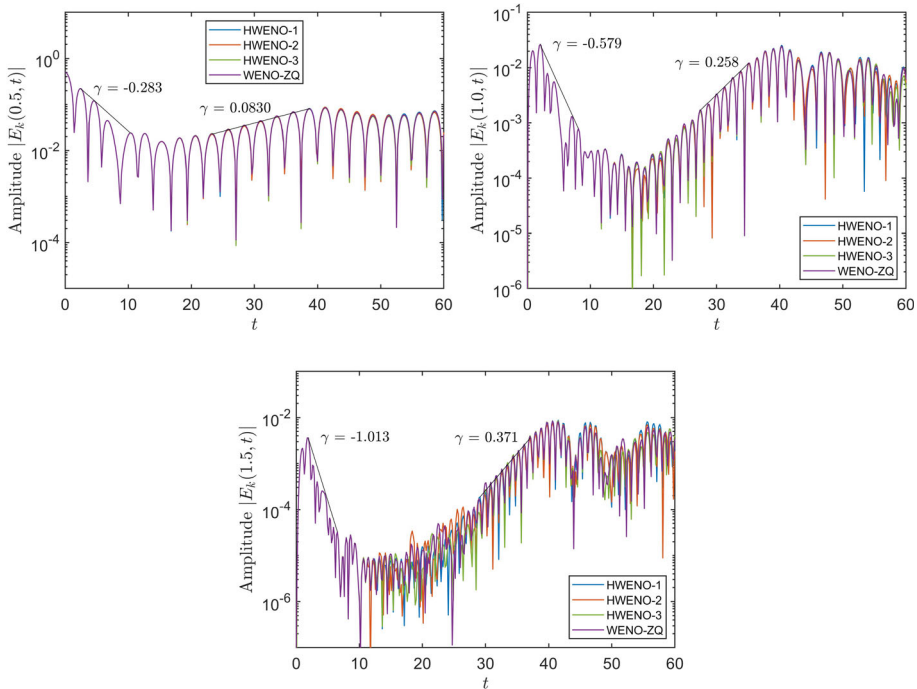


Fig. 14 (Strong Landau damping). Amplitude of the first three Fourier modes of electric field from the SL schemes applying a mesh of 256×256 and a CFL of 10.2

deviations, as simulated by the SL schemes, is elaborated in Fig. 18. These deviations are of similar magnitude and closely align with the levels reported in previous studies [31] and [29]. However, it is important to note that the proposed SL schemes were not originally designed to conserve these quantities. Additionally, the settings of the simulations in the existing literature vary. Therefore, we do not draw specific conclusions about the benefits of using our schemes for the preservation of the L^2 norm, energy, and entropy.

4.3 Guiding Center Vlasov Model

For the guiding center Vlasov model, unless specified, we set $N_x = N_y = 256$, CFL = 10.2, and

$$\Delta t = \text{CFL} / (\max\{|E_1|\}/\Delta x + \max\{|E_2|\}/\Delta y).$$

Example 4.4 (Kelvin–Helmholtz instability problem). Consider the guiding center Vlasov model with the periodic boundary condition and with the following initial condition

$$\rho(x, y, 0) = \sin(y) + 0.015\cos(kx), \quad x \in [0, 4\pi], \quad y \in [0, 2\pi], \quad (4.5)$$

where $k = 0.5$. In Table 4, we show the L^1 errors, L^∞ and corresponding spatial orders of accuracy of the SL schemes. These errors are calculated by comparing the solution with a reference solution obtained through mesh refinement. For this particular problem, the errors and spatial orders of accuracy, which are consistently fourth-order, are nearly identical for the SL HWENO-1 and SL HWENO-2 schemes. However, due to numerical dissipation,

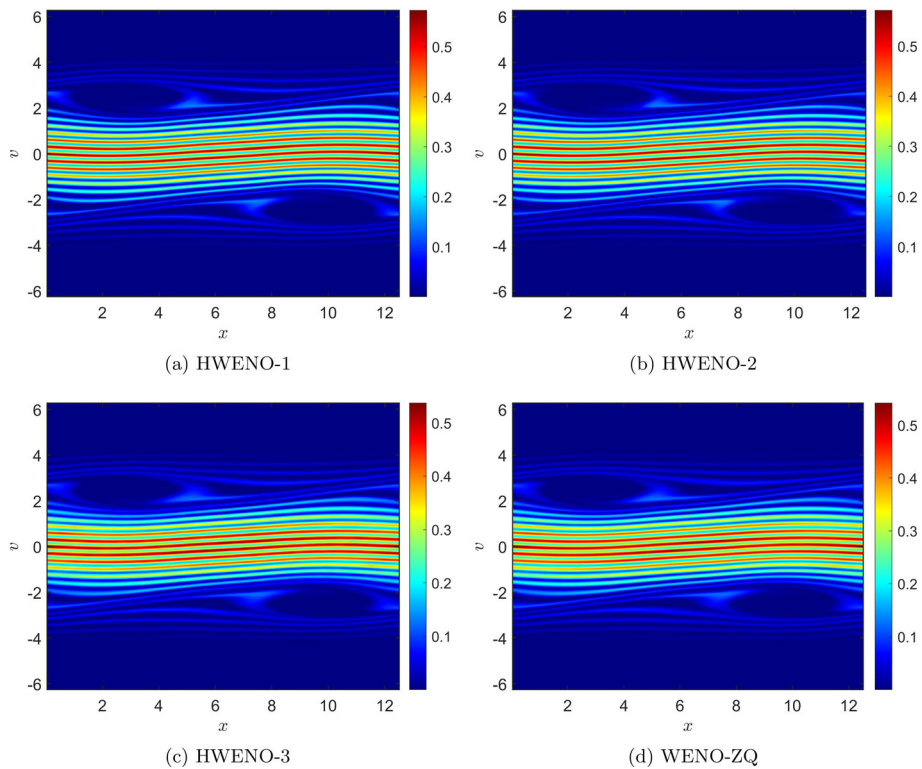


Fig. 15 (Strong Landau damping). Contour plots of the numerical solutions obtained using the SL schemes for the strong Landau damping problem. These plots correspond to $t = 1.5$ and are based on a 128×256 mesh with $\text{CFL} = 10.2$

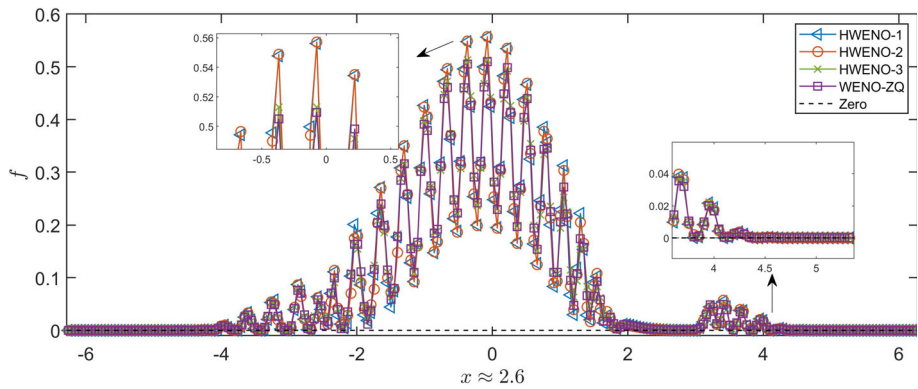


Fig. 16 (Strong Landau damping). Cross-sections of the numerical solutions in Fig. 15 at $x \approx 2.6$

the spatial order data of the SL HWENO-3 and SL WENO-ZQ schemes are not as tidy. A comparison of computational efficiency is provided in Fig. 19, where the SL HWENO-1 and SL HWENO-2 schemes demonstrate greater efficiency for this problem. In Fig. 20, we observe fourth-order temporal accuracy of SL schemes for L^1 error and approximately

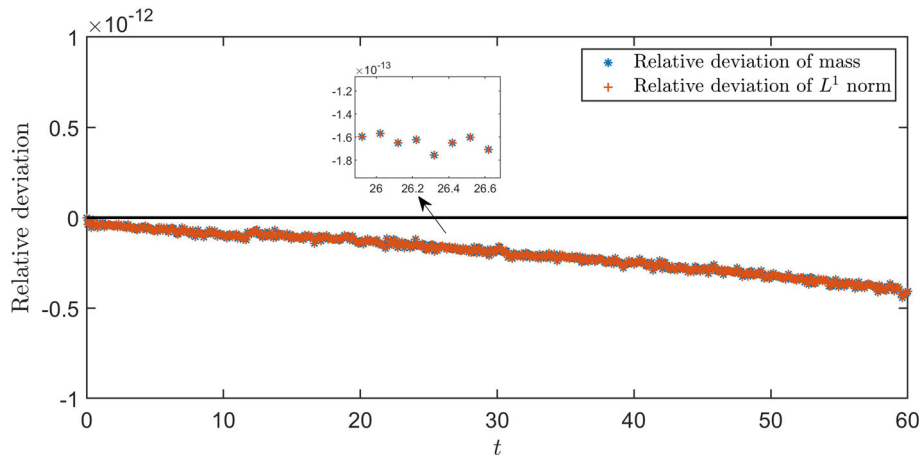


Fig. 17 (Strong Landau damping). Performance of mass conservation and PP properties of the SL HWENO-1 scheme for the strong Landau damping problem with $v_{\max} = 10$. The SL HWENO-1 scheme uses a mesh of 128×256 and a CFL of 10.2

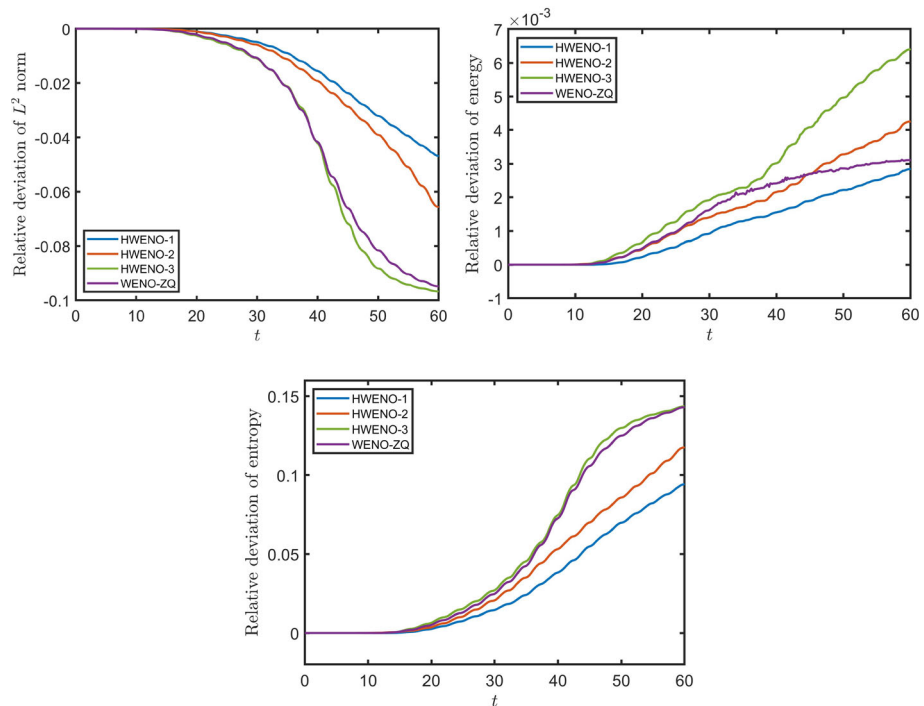
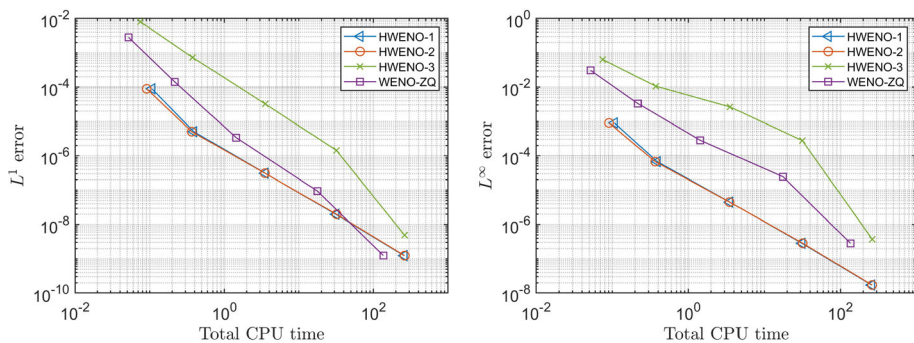
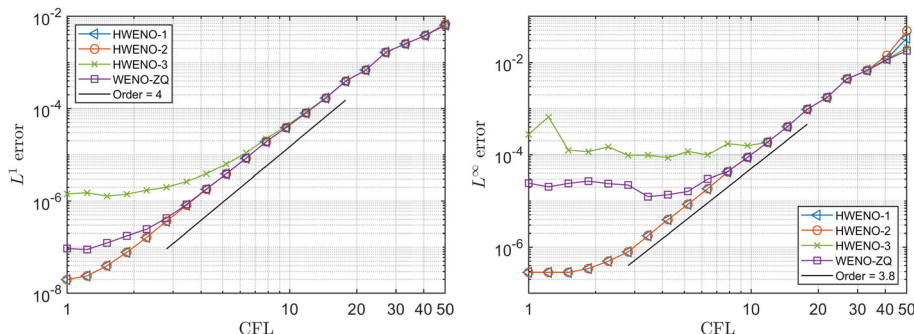


Fig. 18 (Strong Landau damping). Relative deviations of the L^2 norm (top left), energy (top right), and entropy (bottom) simulated by the SL schemes using a mesh of 128×256 and a CFL of 10.2

3.8th-order temporal accuracy for the L^∞ error. Due to dissipation, the SL HWENO-3 scheme exhibits larger L^1 and L^∞ errors when spatial errors dominate the total errors.

Table 4 (Kelvin–Helmholtz instability problem). L^1 errors, L^∞ errors and corresponding spatial orders of accuracy for the SL schemes applied to the Kelvin–Helmholtz instability problem, evaluated at $T = 5$ with $CFL = 10.2$

mesh	SL HWENO-1				SL HWENO-2			
	L^1 error	order	L^∞ error	order	L^1 error	order	L^∞ error	order
16 × 16	8.90E-05	—	9.02E-04	—	8.90E-05	—	9.02E-04	—
32 × 32	5.01E-06	4.15	6.72E-05	3.75	5.01E-06	4.15	6.72E-05	3.75
64 × 64	3.09E-07	4.02	4.48E-06	3.91	3.09E-07	4.02	4.48E-06	3.91
128 × 128	1.98E-08	3.97	2.85E-07	3.98	1.98E-08	3.97	2.85E-07	3.97
256 × 256	1.24E-09	4.00	1.71E-08	4.06	1.24E-09	4.00	1.71E-08	4.06
SL HWENO-3				SL WENO-ZQ				
16 × 16	8.07E-03	—	6.41E-02	—	2.86E-03	—	3.10E-02	—
32 × 32	7.37E-04	3.45	1.06E-02	2.59	1.41E-04	4.34	3.32E-03	3.22
64 × 64	3.22E-05	4.52	2.64E-03	2.00	3.36E-06	5.39	2.81E-04	3.56
128 × 128	1.43E-06	4.49	2.74E-04	3.27	9.41E-08	5.16	2.45E-05	3.52
256 × 256	4.88E-09	8.20	3.74E-07	9.52	1.25E-09	6.24	2.84E-07	6.43

**Fig. 19** (Kelvin–Helmholtz instability problem). Log-log plots comparing CPU times and errors for the SL schemes: L^1 errors (left) and L^∞ errors (right), under the same settings as in Table 4**Fig. 20** (Kelvin–Helmholtz instability problem). Temporal order of accuracy for the SL schemes, evaluated using L^1 error (left) and L^∞ error (right). The simulations use a fix mesh of 128×128 and calculate the errors at $T = 5$

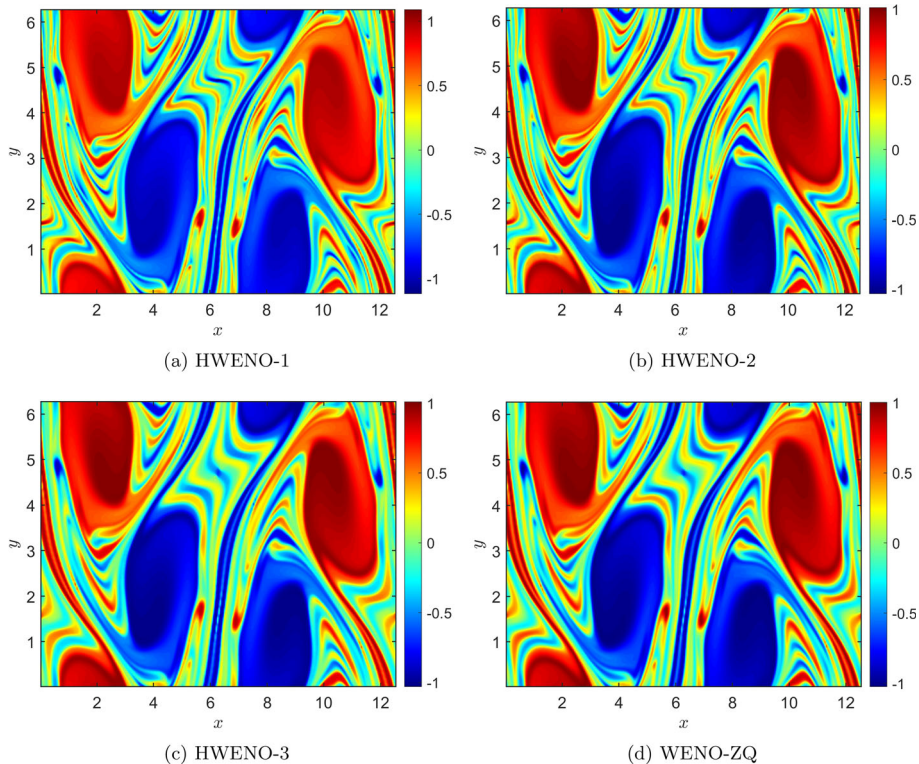


Fig. 21 (Kelvin–Helmholtz instability problem). Contour plots of the numerical solutions obtained using the SL schemes for the Kelvin–Helmholtz instability problem. These plots correspond to $t = 40$ and are based on a 256×256 mesh with $\text{CFL} = 10.2$

In Fig. 21, we present the contour plots of the numerical solutions obtained using the SL schemes at $T = 40$. Cross-sections of these numerical solutions at $y = \pi$ are showcased in Fig. 22. The numerical results align well with those previously reported in the literature [3, 35]. Visually, it is evident that the numerical solution from the SL HWENO-1 scheme captures the most intricate structures. The resolution offered by the SL HWENO-2 scheme is marginally less detailed than that of the SL HWENO-1 scheme. On the other hand, the SL HWENO-3 and SL WENO-ZQ schemes tend to blur some structures in comparison to the first two SL schemes. However, the SL HWENO-1 scheme exhibits distinct upward and downward overshooting compared to the other two schemes, as it overshoots the upper bound of 1.015 and downward overshoots the lower bound of -1.015 . This is notable considering that the guiding center Vlasov model should be preserving its maximum and minimum values.

The Kelvin–Helmholtz instability problem is known to preserve mass, L^p norm, energy, and enstrophy, as described in [35, 36]. In Fig. 23, we illustrate the time evolution of the mass deviation, as well as the relative deviations of the L^1 norm, energy, and enstrophy, as simulated by the SL schemes. We focus on the deviation (rather than the relative deviation) for mass because the total mass of the Kelvin–Helmholtz instability problem is zero. In terms of mass deviation, we observe a magnitude of $O(10^{-11})$ up to $t = 200$ for the SL HWENO schemes, with the SL WENO-ZQ scheme showing a significantly smaller magnitude. For the L^1 norm, energy, and enstrophy, the performance of the SL schemes is consistent and

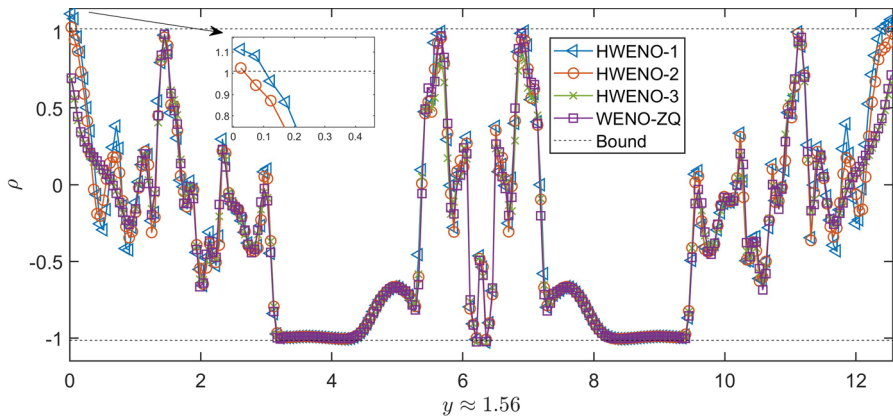


Fig. 22 (Kelvin–Helmholtz instability problem). Cross-sections of the numerical solutions in Fig. 21 at $y \approx 1.56$

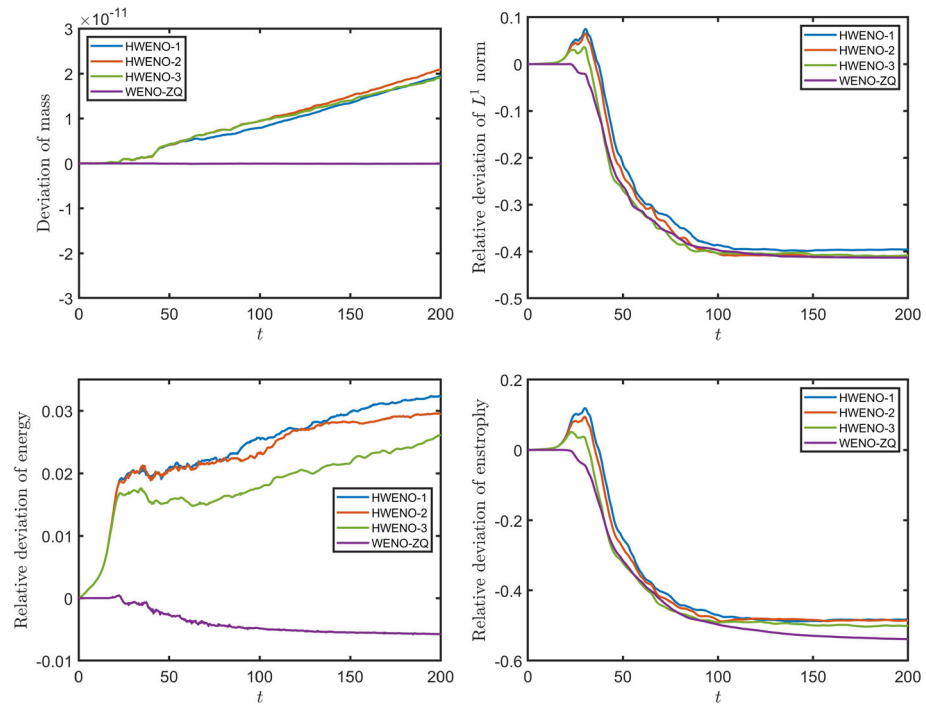


Fig. 23 (Kelvin–Helmholtz instability problem). Deviation of mass (top left), relative deviations of the L^1 norm (top right), energy (bottom left), and enstrophy (bottom right) simulated by the SL schemes using a mesh of 256×256 and a CFL of 10.2

comparable with existing results in the literature [3, 35]. However, it's important to note that the simulation settings in the literature vary significantly, and our proposed schemes are not specifically designed to preserve these quantities. Therefore, we conclude that the performance of the SL schemes is comparable to existing results achieved using schemes not intended for conservation of these quantities.

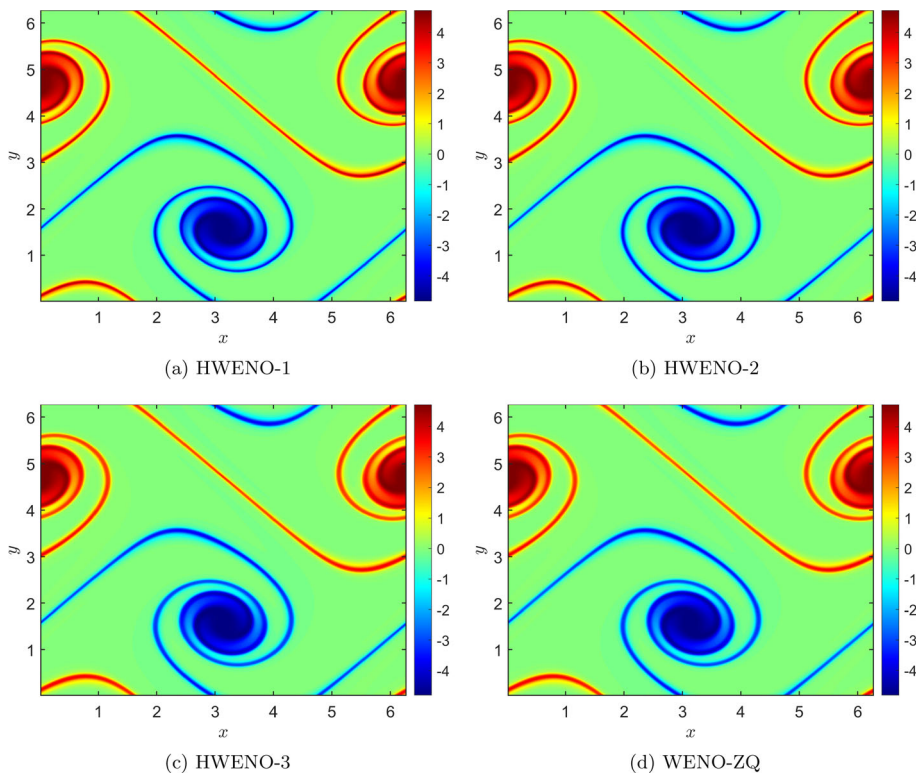


Fig. 24 (Shear flow problem). Contour plots of the numerical solutions obtained using the SL schemes for the shear flow problem. These plots correspond to $t = 8$ and are based on a 256×256 mesh with $\text{CFL} = 10.2$

4.4 Incompressible Euler Equations in Vorticity-Stream Function Formulation

For the 2-D incompressible Euler equations in vorticity-stream function formulation, unless specified, we set $N_x = N_y = 256$, $\text{CFL} = 10.2$, and

$$\Delta t = \text{CFL} / (\max\{u_1\}/\Delta x + \max\{u_2\}/\Delta y).$$

Example 4.5 (Shear flow problem). Consider the incompressible Euler equations in vorticity-stream function formulation in the domain $[0, 2\pi] \times [0, 2\pi]$ with the following initial condition

$$\omega(x, y, 0) = \begin{cases} \delta \cos(x) - \frac{1}{\rho} \operatorname{sech}^2\left(\frac{y-\pi/2}{\rho}\right), & \text{if } y \leq \pi, \\ \delta \cos(x) + \frac{1}{\rho} \operatorname{sech}^2\left(\frac{3\pi/2-y}{\rho}\right), & \text{if } y > \pi, \end{cases} \quad (4.6)$$

where $\delta = 0.05$ and $\rho = \pi/15$, and the periodic boundary condition. In Fig. 24, we show the contour plots of the numerical solutions of the SL schemes at $T = 8$. In Fig. 25, the cross-sections of the numerical solutions in Fig. 24 are provided. From the cross-sections, it is observed that the SL HWENO-3 and SL WENO-ZQ schemes exhibit greater dissipation compared to the other two schemes.

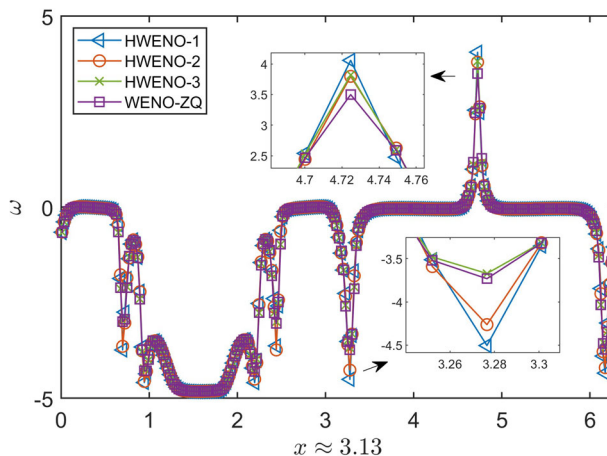


Fig. 25 (Shear flow problem). Cross-sections of the numerical solutions in Fig. 24 at $y \approx 1.56$

5 Conclusion

This paper propose fourth-order SL HWENO schemes without operator splitting for two-dimensional nonlinear Vlasov dynamics. Two new HWENO reconstruction methods are introduced for capturing complicated solution structures without excessive dissipation. The proposed schemes couple the weak formulation of the characteristic Galerkin method with the new HWENO reconstruction methods; the obtained SL HWENO schemes are fourth-order accurate in both space and time, mass conservative, positivity-preserving, and unconditionally stable under a linearized setting. A variety of tests are performed to verify these properties.

Appendix A. Coefficients of $\{q_k(x, y)\}_{k=0}^4$

For $q_0(x, y)$,

$$\begin{aligned}
 a_1^{q_0} &= \bar{u}_{i,j}^n, \quad a_2^{q_0} = 12\tilde{v}_{i,j}^n, \quad a_3^{q_0} = 12\tilde{w}_{i,j}^n, \\
 a_4^{q_0} &= \frac{1}{2}\bar{u}_{i-1,j}^n - \bar{u}_{i,j}^n + \frac{1}{2}\bar{u}_{i+1,j}^n, \\
 a_5^{q_0} &= \frac{1}{4}\bar{u}_{i-1,j-1}^n - \frac{1}{4}\bar{u}_{i+1,j-1}^n - \frac{1}{4}\bar{u}_{i-1,j+1}^n + \frac{1}{4}\bar{u}_{i+1,j+1}^n, \\
 a_6^{q_0} &= \frac{1}{2}\bar{u}_{i,j-1}^n - \bar{u}_{i,j}^n + \frac{1}{2}\bar{u}_{i,j+1}^n, \\
 a_7^{q_0} &= -\frac{5}{11}\bar{u}_{i-1,j}^n + \frac{5}{11}\bar{u}_{i+1,j}^n - \frac{120}{11}\tilde{v}_{i,j}^n, \\
 a_8^{q_0} &= -\frac{1}{4}\bar{u}_{i-1,j-1}^n + \frac{1}{2}\bar{u}_{i,j-1}^n - \frac{1}{4}\bar{u}_{i+1,j-1}^n + \frac{1}{4}\bar{u}_{i-1,j+1}^n - \frac{1}{2}\bar{u}_{i,j+1}^n + \frac{1}{4}\bar{u}_{i+1,j+1}^n, \\
 a_9^{q_0} &= -\frac{1}{4}\bar{u}_{i-1,j-1}^n + \frac{1}{2}\bar{u}_{i,j-1}^n - \frac{1}{4}\bar{u}_{i-1,j+1}^n + \frac{1}{4}\bar{u}_{i+1,j-1}^n - \frac{1}{2}\bar{u}_{i+1,j}^n + \frac{1}{4}\bar{u}_{i+1,j+1}^n, \\
 a_{10}^{q_0} &= -\frac{5}{11}\bar{u}_{i,j-1}^n + \frac{5}{11}\bar{u}_{i,j+1}^n - \frac{120}{11}\tilde{w}_{i,j}^n. \tag{A.1}
 \end{aligned}$$

For $q_1(x, y)$,

$$\begin{aligned} a_1^{q_1} &= \bar{u}_{i,j}^n, \quad a_2^{q_1} = 12\tilde{\bar{v}}_{i,j}^n, \quad a_3^{q_1} = 12\tilde{\bar{w}}_{i,j}^n, \\ a_4^{q_1} &= \bar{u}_{i-1,j}^n - \bar{u}_{i,j}^n + 12\tilde{\bar{v}}_{i,j}^n, \\ a_5^{q_1} &= \bar{u}_{i-1,j-1}^n - \bar{u}_{i,j-1}^n - \bar{u}_{i-1,j}^n + \bar{u}_{i,j}^n, \\ a_6^{q_1} &= \bar{u}_{i,j-1}^n - \bar{u}_{i,j}^n + 12\tilde{\bar{w}}_{i,j}^n. \end{aligned} \quad (\text{A.2})$$

For $q_2(x, y)$,

$$\begin{aligned} a_1^{q_2} &= \bar{u}_{i,j}^n, \quad a_2^{q_2} = 12\tilde{\bar{v}}_{i,j}^n, \quad a_3^{q_2} = 12\tilde{\bar{w}}_{i,j}^n, \\ a_4^{q_2} &= -\bar{u}_{i,j}^n + \bar{u}_{i+1,j}^n - 12\tilde{\bar{v}}_{i,j}^n, \\ a_5^{q_2} &= \bar{u}_{i,j-1}^n - \bar{u}_{i+1,j-1}^n - \bar{u}_{i,j}^n + \bar{u}_{i+1,j}^n, \\ a_6^{q_2} &= \bar{u}_{i,j-1}^n - \bar{u}_{i,j}^n + 12\tilde{\bar{w}}_{i,j}^n. \end{aligned} \quad (\text{A.3})$$

For $q_3(x, y)$,

$$\begin{aligned} a_1^{q_3} &= \bar{u}_{i,j}^n, \quad a_2^{q_3} = 12\tilde{\bar{v}}_{i,j}^n, \quad a_3^{q_3} = 12\tilde{\bar{w}}_{i,j}^n, \\ a_4^{q_3} &= \bar{u}_{i-1,j}^n - \bar{u}_{i,j}^n + 12\tilde{\bar{v}}_{i,j}^n, \\ a_5^{q_3} &= \bar{u}_{i-1,j}^n - \bar{u}_{i,j}^n - \bar{u}_{i-1,j+1}^n + \bar{u}_{i,j+1}^n, \\ a_6^{q_3} &= -\bar{u}_{i,j}^n + \bar{u}_{i,j+1}^n - 12\tilde{\bar{w}}_{i,j}^n. \end{aligned} \quad (\text{A.4})$$

For $q_4(x, y)$,

$$\begin{aligned} a_1^{q_4} &= \bar{u}_{i,j}^n, \quad a_2^{q_4} = 12\tilde{\bar{v}}_{i,j}^n, \quad a_3^{q_4} = 12\tilde{\bar{w}}_{i,j}^n, \\ a_4^{q_4} &= -\bar{u}_{i,j}^n + \bar{u}_{i+1,j}^n - 12\tilde{\bar{v}}_{i,j}^n, \\ a_5^{q_4} &= \bar{u}_{i,j}^n - \bar{u}_{i+1,j}^n - \bar{u}_{i,j+1}^n + \bar{u}_{i+1,j+1}^n, \\ a_6^{q_4} &= -\bar{u}_{i,j}^n + \bar{u}_{i,j+1}^n - 12\tilde{\bar{w}}_{i,j}^n. \end{aligned} \quad (\text{A.5})$$

Appendix B. Numerical Proof of Remark 2.2

Consider the following linear transport equation,

$$u_t + au_x + bu_y = 0 \quad (\text{B.1})$$

with periodic boundary condition. Without loss of generality, we assume that $a > 0$ and $b > 0$. We define $\theta_1 = \frac{a\Delta t}{\Delta x}$ and $\theta_2 = \frac{b\Delta t}{\Delta y}$. Then (2.35) with $H^n(x, y)$ reconstructed by the

linear reconstruction is reorganized as follows:

$$\begin{aligned} \bar{u}_{i,j}^{n+1} = & \frac{1}{\Delta x \Delta y} \left[\int_{x_{i-\frac{1}{2}} - \theta_1 \Delta x}^{x_{i-\frac{1}{2}} - \lfloor \theta_1 \rfloor \Delta x} \int_{y_{j-\frac{1}{2}} - \theta_2 \Delta y}^{y_{j-\frac{1}{2}} - \lfloor \theta_2 \rfloor \Delta y} H^{(i-1-\lfloor \theta_1 \rfloor, j-1-\lfloor \theta_2 \rfloor)}(x, y) dx dy \right. \\ & + \int_{x_{i-\frac{1}{2}} - \lfloor \theta_1 \rfloor \Delta x}^{x_{i-\frac{1}{2}} + (1-\theta_1) \Delta x} \int_{y_{j-\frac{1}{2}} - \theta_2 \Delta y}^{y_{j-\frac{1}{2}} - \lfloor \theta_2 \rfloor \Delta y} H^{(i-\lfloor \theta_1 \rfloor, j-1-\lfloor \theta_2 \rfloor)}(x, y) dx dy \\ & + \int_{x_{i-\frac{1}{2}} - \theta_1 \Delta x}^{x_{i-\frac{1}{2}} - \lfloor \theta_1 \rfloor \Delta x} \int_{y_{j-\frac{1}{2}} - \lfloor \theta_2 \rfloor \Delta y}^{y_{j-\frac{1}{2}} + (1-\theta_2) \Delta y} H^{(i-1-\lfloor \theta_1 \rfloor, j-\lfloor \theta_2 \rfloor)}(x, y) dx dy \\ & \left. + \int_{x_{i-\frac{1}{2}} - \lfloor \theta_1 \rfloor \Delta x}^{x_{i-\frac{1}{2}} + (1-\theta_1) \Delta x} \int_{y_{j-\frac{1}{2}} - \lfloor \theta_2 \rfloor \Delta y}^{y_{j-\frac{1}{2}} + (1-\theta_2) \Delta y} H^{(i-\lfloor \theta_1 \rfloor, j-\lfloor \theta_2 \rfloor)}(x, y) dx dy \right], \end{aligned} \quad (\text{B.2})$$

$$\begin{aligned} \bar{v}_{i,j}^{n+1} = & \frac{1}{\Delta x \Delta y} \left[\int_{x_{i-\frac{1}{2}} - \theta_1 \Delta x}^{x_{i-\frac{1}{2}} - \lfloor \theta_1 \rfloor \Delta x} \int_{y_{j-\frac{1}{2}} - \theta_2 \Delta y}^{y_{j-\frac{1}{2}} - \lfloor \theta_2 \rfloor \Delta y} H^{(i-1-\lfloor \theta_1 \rfloor, j-1-\lfloor \theta_2 \rfloor)}(x, y) \left(\frac{x + \theta_1 \Delta x - x_i}{\Delta x} \right) dx dy \right. \\ & + \int_{x_{i-\frac{1}{2}} - \lfloor \theta_1 \rfloor \Delta x}^{x_{i-\frac{1}{2}} + (1-\theta_1) \Delta x} \int_{y_{j-\frac{1}{2}} - \theta_2 \Delta y}^{y_{j-\frac{1}{2}} - \lfloor \theta_2 \rfloor \Delta y} H^{(i-\lfloor \theta_1 \rfloor, j-1-\lfloor \theta_2 \rfloor)}(x, y) \left(\frac{x + \theta_1 \Delta x - x_i}{\Delta x} \right) dx dy \\ & + \int_{x_{i-\frac{1}{2}} - \theta_1 \Delta x}^{x_{i-\frac{1}{2}} - \lfloor \theta_1 \rfloor \Delta x} \int_{y_{j-\frac{1}{2}} - \lfloor \theta_2 \rfloor \Delta y}^{y_{j-\frac{1}{2}} + (1-\theta_2) \Delta y} H^{(i-1-\lfloor \theta_1 \rfloor, j-\lfloor \theta_2 \rfloor)}(x, y) \left(\frac{x + \theta_1 \Delta x - x_i}{\Delta x} \right) dx dy \\ & \left. + \int_{x_{i-\frac{1}{2}} - \lfloor \theta_1 \rfloor \Delta x}^{x_{i-\frac{1}{2}} + (1-\theta_1) \Delta x} \int_{y_{j-\frac{1}{2}} - \lfloor \theta_2 \rfloor \Delta y}^{y_{j-\frac{1}{2}} + (1-\theta_2) \Delta y} H^{(i-\lfloor \theta_1 \rfloor, j-\lfloor \theta_2 \rfloor)}(x, y) \left(\frac{x + \theta_1 \Delta x - x_i}{\Delta x} \right) dx dy \right], \end{aligned} \quad (\text{B.3})$$

and

$$\begin{aligned} \bar{w}_{i,j}^{n+1} = & \frac{1}{\Delta x \Delta y} \left[\int_{x_{i-\frac{1}{2}} - \theta_1 \Delta x}^{x_{i-\frac{1}{2}} - \lfloor \theta_1 \rfloor \Delta x} \int_{y_{j-\frac{1}{2}} - \theta_2 \Delta y}^{y_{j-\frac{1}{2}} - \lfloor \theta_2 \rfloor \Delta y} H^{(i-1-\lfloor \theta_1 \rfloor, j-1-\lfloor \theta_2 \rfloor)}(x, y) \left(\frac{y + \theta_2 \Delta y - y_j}{\Delta y} \right) dx dy \right. \\ & + \int_{x_{i-\frac{1}{2}} - \lfloor \theta_1 \rfloor \Delta x}^{x_{i-\frac{1}{2}} + (1-\theta_1) \Delta x} \int_{y_{j-\frac{1}{2}} - \theta_2 \Delta y}^{y_{j-\frac{1}{2}} - \lfloor \theta_2 \rfloor \Delta y} H^{(i-\lfloor \theta_1 \rfloor, j-1-\lfloor \theta_2 \rfloor)}(x, y) \left(\frac{y + \theta_2 \Delta y - y_j}{\Delta y} \right) dx dy \\ & + \int_{x_{i-\frac{1}{2}} - \theta_1 \Delta x}^{x_{i-\frac{1}{2}} - \lfloor \theta_1 \rfloor \Delta x} \int_{y_{j-\frac{1}{2}} - \lfloor \theta_2 \rfloor \Delta y}^{y_{j-\frac{1}{2}} + (1-\theta_2) \Delta y} H^{(i-1-\lfloor \theta_1 \rfloor, j-\lfloor \theta_2 \rfloor)}(x, y) \left(\frac{y + \theta_2 \Delta y - y_j}{\Delta y} \right) dx dy \\ & \left. + \int_{x_{i-\frac{1}{2}} - \lfloor \theta_1 \rfloor \Delta x}^{x_{i-\frac{1}{2}} + (1-\theta_1) \Delta x} \int_{y_{j-\frac{1}{2}} - \lfloor \theta_2 \rfloor \Delta y}^{y_{j-\frac{1}{2}} + (1-\theta_2) \Delta y} H^{(i-\lfloor \theta_1 \rfloor, j-\lfloor \theta_2 \rfloor)}(x, y) \left(\frac{y + \theta_2 \Delta y - y_j}{\Delta y} \right) dx dy \right], \end{aligned} \quad (\text{B.4})$$

where $\lfloor \cdot \rfloor$ represents the largest integer smaller than the input number. Now, we assume that

$$\begin{aligned} \bar{u}_{p,q}^n &= \bar{u}^n e^{I\xi_1 p \Delta x} e^{I\xi_2 q \Delta y}, \quad \bar{v}_{p,q}^n = \bar{v}^n e^{I\xi_1 p \Delta x} e^{I\xi_2 q \Delta y}, \\ \bar{w}_{p,q}^n &= \bar{w}^n e^{I\xi_1 p \Delta x} e^{I\xi_2 q \Delta y} \quad \forall p, q, \end{aligned} \quad (\text{B.5})$$

and

$$\begin{aligned} \bar{u}_{i,j}^{n+1} &= \bar{u}^{n+1} e^{I\xi_1 i \Delta x} e^{I\xi_2 j \Delta y}, \quad \bar{v}_{i,j}^{n+1} = \bar{v}^{n+1} e^{I\xi_1 i \Delta x} e^{I\xi_2 j \Delta y}, \\ \bar{w}_{i,j}^{n+1} &= \bar{w}^{n+1} e^{I\xi_1 i \Delta x} e^{I\xi_2 j \Delta y}, \end{aligned} \quad (\text{B.6})$$

where $I = \sqrt{-1}$. Submitting (B.5) and (B.6) into (B.2)–(B.4), we find that

$$\begin{bmatrix} \bar{u}^{n+1} \\ \bar{v}^{n+1} \\ \bar{w}^{n+1} \end{bmatrix} = A(\theta_1, \theta_2, \xi_1, \xi_2) \begin{bmatrix} \bar{u}^n \\ \bar{v}^n \\ \bar{w}^n \end{bmatrix}, \quad (\text{B.7})$$

where $A(\theta_1, \theta_2, \xi_1, \xi_2)$ is the 3×3 amplification matrix. We skip the explicit expression of $A(\theta_1, \theta_2, \xi_1, \xi_2)$ for conciseness since it is very complicated. We denote the spectral radius of $A(\theta_1, \theta_2, \xi_1, \xi_2)$ by $\rho(A(\theta_1, \theta_2, \xi_1, \xi_2))$. With basic algebraic manipulation, we have

$$A(\theta_1, \theta_2, \xi_1, \xi_2) = e^{-I\xi_1\lfloor\theta_1\rfloor\Delta x} e^{-I\xi_2\lfloor\theta_2\rfloor\Delta y} A(\theta_1 - \lfloor\theta_1\rfloor, \theta_2 - \lfloor\theta_2\rfloor, \xi_1, \xi_2). \quad (\text{B.8})$$

Hence, by von Nuemann analysis, it is sufficient to verify that $\rho(A(\theta_1, \theta_2, \xi_1, \xi_2)) \leq 1$ for any $\theta_1, \theta_2 \in [0, 1]$ and $\xi_1 \Delta x, \xi_2 \Delta y \in [0, 2\pi]$. We were not able to find a theoretical expression of $\rho(A(\theta_1, \theta_2, \xi_1, \xi_2))$. We numerically verify this relation by sampling 1000 uniform points over each $\theta_1, \theta_2, \xi_1 \Delta x, \xi_2 \Delta y$ domain. We find that all the $\rho(A(\cdot, \cdot, \cdot, \cdot))$ values computed by the sampling points are not greater than 1, which validates Remark 2.2.

Funding The work of the first and fourth authors was partially supported by the National Key R&D Program of China [Grant number 2022YFA1004501] and the National Natural Science Foundation (China) [Grant Number 12071392]. The work of the second author was partially supported by the National Natural Science Foundation (China) [Grant Number 12201052], the Guangdong Provincial Key Laboratory of Interdisciplinary Research and Application for Data Science, BNU-HKBU United International College, project code 2022B1212010006, and Guangdong Higher Education Upgrading Plan (2021-2025) of “Rushing to the Top, Making Up Shortcomings and Strengthening Special Features” with No. of UICR0400024-21 and No. of R0400001-22. The work of the third author was partially supported by NSF [Grant Numbers NSF-DMS-1818924 and NSF-DMS-2111253], Air Force Office of Scientific Research, United States FA9550-18-1-0257.

Data availability The datasets generated during and/or analyzed during the current study are available from the corresponding author upon reasonable request.

Open Access This article is licensed under a Creative Commons Attribution 4.0 International License, which permits use, sharing, adaptation, distribution and reproduction in any medium or format, as long as you give appropriate credit to the original author(s) and the source, provide a link to the Creative Commons licence, and indicate if changes were made. The images or other third party material in this article are included in the article’s Creative Commons licence, unless indicated otherwise in a credit line to the material. If material is not included in the article’s Creative Commons licence and your intended use is not permitted by statutory regulation or exceeds the permitted use, you will need to obtain permission directly from the copyright holder. To view a copy of this licence, visit <http://creativecommons.org/licenses/by/4.0/>.

References

1. Balsara, D.S., Garain, S., Shu, C.-W.: An efficient class of WENO schemes with adaptive order. *J. Comput. Phys.* **326**, 780–804 (2016)
2. Borges, R., Carmona, M., Costa, B., Don, W.S.: An improved weighted essentially non-oscillatory scheme for hyperbolic conservation laws. *J. Comput. Phys.* **227**(6), 3191–3211 (2008)
3. Cai, X., Boscarino, S., Qiu, J.-M.: High order semi-Lagrangian discontinuous Galerkin method coupled with Runge-Kutta exponential integrators for nonlinear Vlasov dynamics. *J. Comput. Phys.* **427**, 110036 (2021)
4. Cai, X., Guo, W., Qiu, J.-M.: A high order conservative semi-Lagrangian discontinuous Galerkin method for two-dimensional transport simulations. *J. Sci. Comput.* **73**(2–3), 514–542 (2017)
5. Cai, X., Guo, W., Qiu, J.-M.: A high order semi-Lagrangian discontinuous Galerkin method for Vlasov-Poisson simulations without operator splitting. *J. Comput. Phys.* **354**, 529–551 (2018)
6. Cai, X., Qiu, J., Qiu, J.-M.: A conservative semi-Lagrangian HWENO method for the Vlasov equation. *J. Comput. Phys.* **323**, 95–114 (2016)
7. Cai, X., Zhang, X., Qiu, J.: Positivity-preserving high order finite volume HWENO schemes for compressible Euler equations. *J. Sci. Comput.* **68**(2), 464–483 (2016)
8. Castro, M., Costa, B., Don, W.S.: High order weighted essentially non-oscillatory WENO-Z schemes for hyperbolic conservation laws. *J. Comput. Phys.* **230**(5), 1766–1792 (2011)

9. Celledoni, E., Marthinsen, A., Owren, B.: Commutator-free Lie group methods. *Futur. Gener. Comput. Syst.* **19**(3), 341–352 (2003)
10. Dahle, H.K., Ewing, R.E., Russell, T.F.: Eulerian-Lagrangian localized adjoint methods for a nonlinear advection-diffusion equation. *Comput. Methods Appl. Mech. Eng.* **122**(3–4), 223–250 (1995)
11. Du, Z., Li, J.: A Hermite WENO reconstruction for fourth order temporal accurate schemes based on the GRP solver for hyperbolic conservation laws. *J. Comput. Phys.* **355**, 385–396 (2018)
12. Dumbser, M., Balsara, D.S., Toro, E.F., Munz, C.-D.: A unified framework for the construction of one-step finite volume and discontinuous Galerkin schemes on unstructured meshes. *J. Comput. Phys.* **227**(18), 8209–8253 (2008)
13. Frénod, E., Hirstoaga, S.A., Lutz, M., Sonnendrücker, E.: Long time behaviour of an exponential integrator for a Vlasov–Poisson system with strong magnetic field. *Commun. Comput. Phys.* **18**(2), 263–296 (2015)
14. Fu, L.: A very-high-order TENO scheme for all-speed gas dynamics and turbulence. *Comput. Phys. Commun.* **244**, 117–131 (2019)
15. Fu, L., Hu, X.Y., Adams, N.A.: A family of high-order targeted ENO schemes for compressible-fluid simulations. *J. Comput. Phys.* **305**, 333–359 (2016)
16. Fu, L., Hu, X.Y., Adams, N.A.: A new class of adaptive high-order targeted ENO schemes for hyperbolic conservation laws. *J. Comput. Phys.* **374**, 724–751 (2018)
17. Guo, W., Nair, R.D., Qiu, J.M.: A conservative semi-Lagrangian discontinuous Galerkin scheme on the cubed-sphere. *Mon. Weather Rev.* **142**(1), 457–475 (2014)
18. Huang, C.-S., Arbogast, T., Hung, C.-H.: A semi-Lagrangian finite difference WENO scheme for scalar nonlinear conservation laws. *J. Comput. Phys.* **322**, 559–585 (2016)
19. Indra, W., Yanuar, Engkos, K.: A fifth-order Hermite targeted essentially non-oscillatory schemes for hyperbolic conservation laws. *J. Sci. Comput.* **87**, 69 (2021)
20. Jiang, G.-S., Shu, C.-W.: Efficient implementation of weighted ENO schemes. *J. Comput. Phys.* **126**(1), 202–228 (1996)
21. Knorr, G.: The integration of the Vlasov equation in configuration space. *J. Comput. Phys.* **22**(3), 330–351 (1976)
22. Lee, D., Lowrie, R.B., Petersen, M.R., Ringler, T.D., Hecht, M.W.: A high order characteristic discontinuous Galerkin scheme for advection on unstructured meshes. *J. Comput. Phys.* **324**, 289–302 (2016)
23. Liu, X.-D., Osher, S., Chan, T.: Weighted essentially non-oscillatory schemes. *J. Comput. Phys.* **115**(1), 200–212 (1994)
24. Morton, K.W.: On the analysis of finite volume methods for evolutionary problems. *SIAM J. Numer. Anal.* **35**(6), 2195–2222 (1998)
25. Nakamura, T., Yabe, T.: Cubic interpolated propagation scheme for solving the hyper-dimensional Vlasov–Poisson equation in phase space. *Comput. Phys. Commun.* **120**(2–3), 122–154 (1999)
26. Qiu, J., Shu, C.-W.: Hermite WENO schemes and their application as limiters for Runge–Kutta discontinuous Galerkin method: one-dimensional case. *J. Comput. Phys.* **193**(1), 115–135 (2004)
27. Qiu, J., Shu, C.-W.: Hermite WENO schemes and their application as limiters for Runge–Kutta discontinuous Galerkin method II: Two dimensional case. *Computers & Fluids* **34**(6), 642–663 (2005)
28. Qiu, J.-M., Shu, C.-W.: Conservative high order semi-Lagrangian finite difference WENO methods for advection in incompressible flow. *J. Comput. Phys.* **230**(4), 863–889 (2011)
29. Qiu, J.-M., Shu, C.-W.: Positivity preserving semi-Lagrangian discontinuous Galerkin formulation: theoretical analysis and application to the Vlasov–Poisson system. *J. Comput. Phys.* **230**(23), 8386–8409 (2011)
30. Restelli, M., Bonaventura, L., Sacco, R.: A semi-Lagrangian discontinuous Galerkin method for scalar advection by incompressible flows. *J. Comput. Phys.* **216**(1), 195–215 (2006)
31. Rossmanith, J.A., Seal, D.C.: A positivity-preserving high-order semi-Lagrangian discontinuous Galerkin scheme for the Vlasov–Poisson equations. *J. Comput. Phys.* **230**(16), 6203–6232 (2011)
32. Russell, T.F., Celia, M.A.: An overview of research on Eulerian–Lagrangian localized adjoint methods (ELLAM). *Adv. Water Resour.* **25**(8–12), 1215–1231 (2002)
33. Shu, C.-W.: Essentially non-oscillatory and weighted essentially non-oscillatory schemes for hyperbolic conservation laws. In: Advanced Numerical Approximation of Nonlinear Hyperbolic Equations, pp. 325–432. Springer (1998)
34. Sirajuddin, D., Hitchon, W.N.: A truly forward semi-Lagrangian WENO scheme for the Vlasov–Poisson system. *J. Comput. Phys.* **392**, 619–665 (2019)
35. Xiong, T., Russo, G., Qiu, J.: Conservative multi-dimensional semi-Lagrangian finite difference scheme: stability and applications to the kinetic and fluid simulations. *J. Sci. Comput.* **79**, 1241–1270 (2019)
36. Yang, C., Filbet, F.: Conservative and non-conservative methods based on Hermite weighted essentially non-oscillatory reconstruction for Vlasov equations. *J. Comput. Phys.* **279**, 18–36 (2014)

37. Zhang, X., Shu, C.-W.: On maximum-principle-satisfying high order schemes for scalar conservation laws. *J. Comput. Phys.* **229**(9), 3091–3120 (2010)
38. Zhao, Z., Chen, Y., Qiu, J.: A hybrid Hermite WENO scheme for hyperbolic conservation laws. *J. Comput. Phys.* **405**, 109175 (2020)
39. Zhao, Z., Qiu, J.: A Hermite WENO scheme with artificial linear weights for hyperbolic conservation laws. *J. Comput. Phys.* **417**, 109583 (2020)
40. Zheng, N., Cai, X., Qiu, J.-M., Qiu, J.: A conservative semi-Lagrangian hybrid Hermite WENO scheme for linear transport equations and the nonlinear Vlasov–Poisson system. *SIAM J. Sci. Comput.* **43**(5), A3580–A3606 (2021)
41. Zheng, N., Cai, X., Qiu, J.-M., Qiu, J.: A fourth-order conservative semi-Lagrangian finite volume WENO scheme without operator splitting for kinetic and fluid simulations. *Comput. Methods Appl. Mech. Eng.* **395**, 114973 (2022)
42. Zhu, J., Qiu, J.: A new fifth order finite difference WENO scheme for solving hyperbolic conservation laws. *J. Comput. Phys.* **318**, 110–121 (2016)

Publisher's Note Springer Nature remains neutral with regard to jurisdictional claims in published maps and institutional affiliations.